Bioactive Materials 6 (2021) 503–519

Contents lists available at ScienceDirect

Bioactive Materials

journal homepage: http://www.keaipublishing.com/biomat

Stepwise 3D-spatio-temporal magnesium cationic niche: Nanocomposite scaffold mediated microenvironment for modulating intramembranous ossification

Jie Shen[a,b,1], Bo Chen[a,c,1], Xinyun Zhai[d], Wei Qiao[a,b], Shuilin Wu[e,f], Xuanyong Liu[g,h], Ying Zhao[i], Changshun Ruan[i], Haobo Pan[i], Paul K. Chu[j], Kenneth M.C. Cheung[a,b], Kelvin W.K. Yeung[a,b,*]

[a] Department of Orthopaedics and Traumatology, The University of Hong Kong, Hong Kong, China
[b] Shenzhen Key Laboratory for Innovative Technology in Orthopaedic Trauma, Department of Orthopaedics and Traumatology, the University of Hong Kong-Shenzhen Hospital, Shenzhen, China
[c] Shanghai Institute of Traumatology and Orthopaedics, Shanghai Key Laboratory for Prevention and Treatment of Bone and Joint Diseases, Ruijin Hospital, School of Medicine, Shanghai Jiaotong University, Shanghai, China
[d] School of Materials Science and Engineering, Nankai University, Tianjin, China
[e] School of Materials Science & Engineering, the Key Laboratory of Advanced Ceramics and Machining Technology by the Ministry of Education of China, Tianjin University, Tianjin, China
[f] Ministry-of-Education Key Laboratory for the Green Preparation and Application of Functional Materials, Hubei Key Laboratory of Polymer Materials, School of Materials Science & Engineering, Hubei University, Wuhan, China
[g] State Key Laboratory of High Performance Ceramics and Superfine Microstructure, Shanghai Institute of Ceramics, Chinese Academy of Sciences, Shanghai, China
[h] Cixi Center of Biomaterials Surface Engineering, Shanghai Institute of Ceramics, Chinese Academy of Sciences, Ningbo, China
[i] Center for Human Tissues and Organs Degeneration, Shenzhen Institutes of Advanced Technology, Chinese Academy of Sciences, Shenzhen, China
[j] Department of Physics, Department of Materials Science & Engineering, and Department of Biomedical Engineering, City University of Hong Kong, Hong Kong, China

ARTICLE INFO

Keywords:
Nanocomposite
Magnesium ion
Microenvironment
3D scaffold
Bone tissue regeneration

ABSTRACT

The fate of cells and subsequent bone regeneration is highly correlated with temporospatial coordination of chemical, biological, or physical cues within a local tissue microenvironment. Deeper understanding of how mammalian cells react to local tissue microenvironment is paramount important when designing next generation of biomaterials for tissue engineering. This study aims to investigate that the regulation of magnesium cationic (Mg^{2+}) tissue microenvironment is able to convince early-stage bone regeneration and its mechanism undergoes intramembranous ossification. It was discovered that moderate Mg^{2+} content niche (~4.11 mM) led to superior bone regeneration, while Mg^{2+}-free and strong Mg^{2+} content (~16.44 mM) discouraged cell adhesion, proliferation and osteogenic differentiation, thereby bone formation was rarely found. When magnesium ions diffused into free Mg zone from concentrated zone in late time point, new bone formation on free Mg zone became significant through intramembranous ossification. This study successfully demonstrates that magnesium cationic microenvironment serves as an effective biochemical cue and is able to modulate the process of bony tissue regeneration. The knowledge of how a Mg^{2+} cationic microenvironment intertwines with cells and subsequent bone formation gained from this study may provide a new insight to develop the next generation of tissue-repairing biomaterials.

1. Introduction

Local tissue microenvironment which is created by biochemical, biophysical or other factors tightly regulates cellular behaviors [1–3]. The diverse cues within a microenvironment synergistically or antagonistically interact in an intricate approach to enhance the cellular proliferation that can lead to accelerated tissue repair, while restricting cellular differentiation often results in jeopardized regenerative processes [4,5]. Therefore, precise control of the spatial and temporal factors inside a microenvironment is crucial throughout the

Peer review under responsibility of KeAi Communications Co., Ltd.
* Corresponding author. Department of Orthopaedics and Traumatology, the University of Hong Kong, Hong Kong, China
E-mail address: wkkyeung@hku.hk (K.W.K. Yeung).
[1] Jie Shen and Bo Chen contributed equally to this work.

https://doi.org/10.1016/j.bioactmat.2020.08.025
Received 25 March 2020; Received in revised form 28 August 2020; Accepted 29 August 2020

entire process of tissue regeneration. Gaining insight into the interactions between microenvironments and cells is thus important to guiding the development of sophisticated biomaterials for regenerative medical applications [6,7]. This has been exemplified by biomaterials with accurately regulated scaffold architectures and compositions that can control the temporospatial release of related factors, and respond dynamically to signals present in a microenvironment [8–10].

As one of the soluble cues, the bioinorganic magnesium cation (Mg^{2+}), which plays an important role in numerous cellular functions and is naturally found in bone tissues, is essential in the regulation of protein synthesis, the activation of enzymes and the formation of bone [11,12]. The stimulation of bone growth by Mg^{2+} has been extensively investigated, mainly with regard to enhancing osteoblastic and compromising osteoclastic activities [13,14]. Studies have demonstrated that not only can Mg^{2+} improve the adhesion of human bone-derived cells and enhance bone healing by increasing the attachment and differentiation of osteoblastic cells [15,16], but it can also aid in the osteogenic differentiation of stem cells through increasing the neuropeptide neuronal calcitonin gene-related polypeptide-α [17]. Mg^{2+} is an important bivalent ion in the formation of biological apatite [18], and other studies have shown that it is actively engaged in the cellular mineralization that regulates bone resorption and formation [19]. Mg^{2+} deficiency, however, impairs bone growth and increases bone resorption in trabecular tissue [20,21]. Nevertheless, all studies have affirmed the importance of Mg^{2+} in bone cell activities.

To date, biomaterials have become effective mediums for regulating the cellular microenvironment in the areas of tissue engineering, chemical testing, and drug delivery [22,23]. Although significant effort has been devoted to the revelation of mechanisms and the fabrication of novel biomaterials that lead to better control and regulation of cell-microenvironment interactions, such works are still far from being optimum. A deeper understanding of the quantitative and qualitative biological response of cells within their microenvironments will be necessary for guiding future biomaterial design and preparation [24,25].

Therefore, to further understand the effect of the magnesium ionic microenvironment on osteoblastic cell behaviors and bone tissue regeneration, after successfully established gradient of Mg^{2+} microenvironments by nanocomposites comprising surface-treated nanomagnesium oxide (MgO) and biodegradable-polymer polycaprolactone (PCL), a series of co-disks, which are composed of a semicircular PCL disk and a semicircular composite disk, are employed in this study and are followed by *in vitro* and *in vivo* investigations. We believe that in-depth knowledge of the magnesium ionic microenvironment-cell interactions and subsequent bone formation acquired from this study will bring us one step closer to improved design and fabrication of biomaterials for tissue regeneration.

2. Materials and methods

2.1. Effect of the magnesium ion on cell adhesion, migration and proliferation

2.1.1. Cell adhesion

Mouse-derived pre-osteoblast cell MC3T3-E1 was used in this study. High-glucose Dulbecco's modified Eagle's medium (DMEM) (Invitrogen, USA) was used to culture the cells. It was replenished with 100 mg/L of streptomycin and 100 U/ml of penicillin, 10% fetal bovine serum (Gibco, Australia) and 2 mM L-glutamine. The incubation atmosphere contained 95% air and 5% CO_2 with the temperature of 37 °C.

To observe the early-stage cell adhesion behaviors in mediums with different concentrations of Mg^{2+}, a total of five different concentrations, including magnesium-free and normal DMEM mediums as control groups, containing mediums were used in the following assays. A time-lapse phase-contrast microscope (PerkinElmer, USA) was first used. Live MC3T3-E1 pre-osteoblast cells were seeded with a cell density of 3×10^4 cells/cm^2 in a 6-well cell chamber (ibidi, Germany) using mediums with different concentrations of Mg^{2+} (0, 20, 100, 200, and 400 ppm, i.e. 0, 0.82, 4.11, 8.22 and 16.44 mM prepared with magnesium chloride). Time-lapse images were captured using the MetaMorph image system 7.8.2.0 with an X, Y motorized scanning stage. The temperature of the cell chamber and the objective were maintained at 37 °C with an atmosphere of 95% air and 5% CO_2 in an incubation chamber during the experiment period. A series of time-lapse images was taken after the cells were seeded for one, two, four and 6 h.

After the time-lapse microscopic observation, the early-stage cell adhesion behaviors of the MC3T3-E1 pre-osteoblast cells in mediums with different concentrations of Mg^{2+} were further assessed via fluorescent staining. The pre-osteoblast cells were seeded with a cell density of 3×10^4 cells/cm^2 in the DMEM mediums with different concentrations of Mg^{2+} (0, 20, 100, 200, and 400 ppm). After incubation for one or 6 h the cells were washed with phosphate-buffered saline (PBS) and fixed using 10% neutral buffered formalin for 1 h, followed by a brief wash again with PBS. Then the nuclei of the cells were stained by Hoechst 33342 (Thermo Fisher, USA), the cytoskeleton protein F-actin was stained with the rhodamine-phalloidin fluorescein dye (Thermo Fisher, USA), and the cells were observed via fluorescence microscopy (Niko ECL IPSE 80i, Japan).

2.1.2. Cell migration

Similar to the cell adhesion experiments, to record cell migration, live MC3T3-E1 pre-osteoblast cells were seeded with a cell density of 3×10^4 cells/cm^2 in a 6-well cell chamber (ibidi, Germany) using mediums with different concentrations of Mg^{2+} (0, 20, 100, 200, and 400 ppm). The cell chamber was localized on a phase-contrast microscope (PerkinElmer, USA) with an attached CCD camera (CRCA 03G). Time-lapse images were captured using the MetaMorph image system 7.8.2.0 with an X, Y motorized scanning stage. The temperature of the cell chamber and the objective were maintained at 37 °C with an atmosphere of 95% air and 5% CO_2 in an incubation chamber during the experiment period. For each well/concentration, eight viewing fields under a 20 × objective were chosen. A series of time-lapse images was taken in 20-min intervals for 12 h.

The time-lapse images, were then imported into ImageJ to quantify the cell migration. The MtrackJ tool was used to mark the tracks of the cells, and the Chemotaxis tool was adopted to plot the pathways. The trajectory velocity (the trajectory distance divided by the time) which is a parameter of cell mobility was then quantified. The following criteria were sued to choose the cells to track: first, only live cells which had good light reflection and shapes were chosen for the analysis; second, cells which interfered with each other's movement were eliminated; third, cells remained visible during the entire period of observation. At least 50 cells were chosen from each group.

2.1.3. Cell proliferation

Cell proliferation property of the pre-osteoblasts MC3T3-E1 in high-glucose DMEM medium with different concentration of Mg^{2+} was investigated by using a BrdU assay (Roche, USA). In 96-well plates, the cell was seeded with a density of 3×10^4 cells/cm^2 using mediums with different concentrations of Mg^{2+} (0, 20, 100, 200, and 400 ppm) for 12, 24, and 72 h. A BrdU labeling solution was then added 10 μL/well to each well according to the manufacturer's protocol. The pre-osteoblasts that just labeled were incubated next using peroxidase-conjugated antibodies. Lastly, after adding a kit-provided substrate solution, the developed color was determined by a photometer at 370 nm wavelength with a reference wavelength of 492 nm.

2.2. Preparation of surface-treated magnesium oxide nanoparticles

Similar to our previous study [26], the nano-MgO (Aladdin Reagent Inc, China) was used after the surface modification. The nano-MgO

surface-treatment procedure was as follow: 20 g of the untreated MgO particles were added to 4 mL of propylamine together with 6 mL of 3-(Trimethoxysilyl)propyl methacrylate (TMSPM, Sigma-Aldrich, USA) and 200 mL cyclohexane. During mixing, the reacting temperature was kept at 80 °C then the mixture was stirred for 3 h continuously. In the end, surface-coated MgO nanoparticles (T-MgO) were collected after filtration and overnight vacuum drying. The molecular reaction between the MgO and TMSPM coupling agent was demonstrated in Fig. 2a. The structure of the untreated nano-MgO (U–MgO) was observed via transmission electron microscope (TEM, FEI Tecnai G2 20 S-TWIN, USA) and selected area electron diffraction (SAED). The structure of the T-MgO was characterized by Raman spectroscopy and Fourier transform infrared spectroscopy (FT-IR).

2.3. Preparation of PCL/T-MgO composite materials

Polycaprolactone/magnesium oxide (PCL/T-MgO) nanocomposite materials were prepared by incorporating different ratio of surface-treated MgO nanoparticles into biodegradable macromolecule PCL (Sigma-Aldrich, USA, average molecular weight 80,000 g/mol) via a solution blending method in a mixer with the temperature of 60 °C. Three different amounts of magnesium oxide (1 g, 2 g and 6 g, T-Mild, T-Moderate and T-Strong) were added into 10 g of PCL, respectively (the preparing process is demonstrated in Fig. 2a and the formulations of PCL/T-MgO composites are as shown in Table 1). The structure of the composite was also characterized by the FT-IR.

2.4. Interface observation of the composites

To monitor the distribution of magnesium element in all the PCL/T-MgO composites, the cross sections morphologies and magnesium element distribution of the materials were observed by scanning electron microscopy (SEM, Hitachi S-4800 FEG, Japan) and energy-dispersive x-ray spectroscopy (EDS), respectively.

2.5. Mechanical property of the composites

Material Testing System (MTS) 858.02 Mini Bionix testing machine (MTS Systems Corporation, USA) was used to characterize the compression modulus of the PCL and PCL/T-MgO composites according to the protocol of ASTM D695-15. Ten rod-shape specimens in each group with the diameter of 3 mm and length of 6 mm were measured with the testing speed of 1 mm/min.

2.6. Ion-releasing profile of the composites

To working out the accumulative release profiles of magnesium ion (Mg^{2+}) from PCL/T-MgO composites, an immersion test was performed. The measuring process of the accumulative Mg^{2+} concentrations was as follow: disk samples (weight of disk sample = 0.05 g, diameter = 1 cm) of each composite were immersed individually into capsules which contain 10 mL of simulated body fluid (SBF). The capsules were then incubated for 1, 3, 7, 15 and 30 days at 37 °C, respectively. The accumulative Mg^{2+} concentration of each sample was measured via inductively coupled plasma optical emission spectrometry (ICP-OES) (PerkinElmer, Optima 2100DV) at each time point. Therefore, the correlation between immersion time and Mg^{2+} dissolution was established.

Table 1
Formulations of PCL/T-MgO composites.

PCL: T-MgO (grams/grams)	10 : 1	10 : 2	10 : 6
Molality	2.48 Mol/Kg	4.96 Mol/Kg	14.88 Mol/Kg
Sample	T-Mild	T-Moderate	T-Strong

Another immersion test was also carried out to monitor the amounts of Mg^{2+} released from the PCL/T-MgO composites in DMEM culture medium. The well plates with the composites immersed in DMEM were placed in an incubator for seven different time points (1, 2, 4, 8, 12, 24, and 48 h). At each time point, the Mg^{2+} ions were also measured using ICP-OES.

2.7. In vitro characterizations of the composites

2.7.1. Cell proliferation on composites

The BrdU assay was also used to investigate the cell proliferation property of MC3T3-E1 pre-osteoblasts on different composites. Similar to the method mentioned in 2.1.3, the cells were seeded with a density of 3×10^4 cells/cm^2 on the composite samples for 24 and 72 h. Then, same procedures were performed to work out the BrdU activities.

2.7.2. Cell viabilities on composites

Human primary mesenchymal stem cells (MSCs, Cyagen Biosciences, China) were used in this research. The replenished α-MEM medium with 100 mg/L of streptomycin and 100 U/mL of penicillin, 10% fetal bovine serum (Gibco, Australia) and 2 mM L-glutamine was used to culture these cells. The incubation temperature is 37 °C with an atmosphere of 95% air and 5% CO2.

A CCK-8 assay was performed to investigate the cell viabilities of the PCL and composites to the MSCs. The cells were seeded with a cell density of 3×10^4 cells/cm^2 in 96-well plates on the samples for 1 and 3 days. Then the culture medium was replaced with 100 μL of the α-MEM medium and 10 μL of the CCK-8 solution (Dojindo, Japan) were added to each well incubated at 37 °C for 2 h. Finally, the optical density (OD) values were recorded by a microplate photometer at a 450 nm wavelength with a reference wavelength of 620 nm to determine the cell viability.

2.7.3. Morphological observation of MSCs on composites

The morphology of MSCs presented on different materials were observed using SEM (Hitachi S–3400 N variable pressure SEM). The sample disks were first placed into a 96-well plate, and the pre-MSCs were seeded with a cell density of 3×10^4 cells/cm^2, then cultured same as above. After incubation for one day, the cells were washed with PBS and fixed using 10% neutral buffered formalin for 1 h, followed by a brief wash again with PBS. Specimens were then dehydrated using an increasing concentration series of ethanol washes (30%, 50%, 70% and 90%, each concentration twice) then thrice in absolute ethanol before they were subjected to the air-dry process. Next, they were mounted on an aluminum stage and coated with platinum in a sputter coater (Baltec SCD 005 Sputter Coater) before viewing.

2.7.4. Osteogenic differentiation

Osteoinductivity of the PCL/T-MgO composites to murine cells and human MSCs were assessed by the alkaline phosphatase (ALP, Stanbio, USA) assay after 3-, 7- and 14-days culturing. The pre-osteoblast cell MC3T3-E1 or MSCs with the density of 4×10^4 cells/cm^2 were incubated on the composites for 24 h after seeding in the culture medium. Then an osteogenic induction medium which containing 10 mM of β-glycerol phosphate (β-GP, MP Biomdicals, France), 100 nM of dexamethasone (Dex, Santa Cruz, UK), and 50 μg/mL ascorbic acid (AA, Sigma-Aldrich, USA) was used to replace the culture medium before incubated for further 3, 7 and 14 days. At each time point, the cells were washed by PBS for three times followed by cytolysis process at 4 °C using 0.1% Triton X-100 for 30 min. The lysates were then centrifuged at 4 °C with the speed of 3000 rpm for 15 min. The ALP reagent containing p-nitrophenyl phosphate was employed to measure the ALP activity of each sample using 10 μL of the supernatant by a colorimetric assay which recorded the absorbance values at 405 nm wavelength. Finally, the measured ALP value was normalized to the total protein which acquired by a protein assay (Bio-Rad, USA).

2.7.5. Cell mineralization

Alizarin red S (ARS) staining was employed to evaluate the capability of mineralization of the pre-osteoblast cells and MSCs cultured on the PCL and different composites. The culturing condition of the ARS test was identical to that of the ALP assay. And the samples were fixed and stained after 14, 17 and 21 days cultured in the osteogenic induction medium. For the staining, the specimens were washed two times with PBS at each time point. After fixed for 1 h by 10% neutral buffered formalin, the specimens were then washed again with acidic PBS (pH ~ 4.2) for two times. After washing, they were stained for 15 min at room temperature by an ARS staining solution (1%, Sigma-Aldrich, USA). Finally, after a 10% acetic acid was added for 30 min shaking, the absorbance of those extracts was evaluated by a photometer at 450 nm wavelength.

2.8. Local magnesium ionic microenvironment in osteoblastic activities

2.8.1. Preparation of co-disks

To study the effect of the local magnesium ionic microenvironment on osteogenic cell behaviors, a series of PCL/composite co-disks were prepared. The preparation process for the co-disks is illustrated in Fig. 5a. In brief, the PCL or composite was first placed onto a glass slide heated by a hot plate at 80 °C. A sample disk with a 6 mm diameter was prepared using the pressing plate method, then it was cut into a semicircular shape. Finally, the PCL and composite semicircular disks were splice together at 60 °C to obtain the co-disk.

2.8.2. Cell morphology observation

Enhanced green fluorescent protein osteoblasts (eGFPOB) and MC3T3-E1 pre-osteoblast cells derived from mice were used in this study. The culturing conditions were identical to that of the cell adhesion assay. To examine the cell morphologies shown on the co-disks, 3×10^4 cells/cm^2 eGFPOB cells were seeded onto the surfaces of different specimens. After culturing for one, two or three days, the adhesion morphologies of the eGFPOB cells were observed via fluorescence microscopy (Niko ECL IPSE 80i, Japan).

Like the method that mentioned above, the MC3T3-E1 pre-osteoblast cell morphologies presented on different co-disks were also observed using SEM (Hitachi S–3400 N variable pressure SEM). The co-disks were first placed into a 96-well plate, and the pre-osteoblast cells were seeded with a cell density of 3×10^4 cells/cm^2, then cultured same as above. After incubation for three days, the samples were gone through the dehydration and coating processes before viewing.

Fluorescent staining was used to further observe the cell morphologies and quantitatively analyze cell number on the co-disks. Similar to the procedure for the SEM observation, after incubation for three days the cells were washed with PBS and fixed using 10% neutral buffered formalin for 1 h, followed by a brief wash again with PBS. Then the nuclei of the cells were stained by Hoechst 33342 (Thermo Fisher, USA), the cytoskeleton protein F-actin was stained with the rhodamine-phalloidin fluorescein dye (Thermo Fisher, USA), and the cells were observed via fluorescence microscopy (Niko ECL IPSE 80i, Japan). Quantitative analysis was then performed using ImageJ software.

2.8.3. Monitoring of local spatial distribution of magnesium ions

The scanning ion-selective electrode technique (SIET) (BIO-001A, Younger USA Sci. and Tech. Corp.; Amherst, MA, USA) as described in previously research [27] with small modifications by the Xu-Yue company (Beijing, China) was used to measure the net fluxes of Mg^{2+} over the surface of all the co-disks. A selective microelectrode for Mg^{2+} was used sequentially to map the net fluxes of Mg^{2+} at a distance of 50 μm above the composite surfaces on a 5 × 10 grid after a 30 min immersion in the measuring solution (8.06 mM $Na_2HPO_4{\cdot}7H_2O$, 1.47 mM KH_2PO_4, 137.93 mM NaCl, 2.67 mM KCl, 1.00 mM $MgCl_2{\cdot}7H_2O$). The obtained data were then analyzed and converted to specific ion outflow (pmol·cm^{-2}·s^{-1}).

2.9. In vivo studies

2.9.1. The fabrication of 3D-printed scaffolds and surgical procedures

The preparation process of the 3D-printed scaffold was based on a low-temperature extrusion-based additive manufacturing technique. Briefly, 30% (weight percent, wt%) of the PCL or the composites were first homogeneously dissolved in 1,4-Dioxane (Sigma, USA) to form gel-like solutions. After loaded the solutions into a specific syringe barrel, the scaffolds were printed via an extrusion-based rapid-prototyping machine (gesim biosacffolder2.1, Germany) on a −20 °C cooling stage with the syringe barrel heated to 40 °C. All of the scaffolds were printed layer-by-layer using a computer-aided deposition approach. After printing, they were then lyophilized for 72 h. Surface morphology of the PCL and composite scaffolds were observed using SEM (Zeiss LEO 1530 FEG SEM, Germany).

The checked protocol for surgical and postoperative care of the rat study were fulfilled according to the requests stated by the University Ethics Committee of the University of Hong Kong as well as the Licensing Office of the Department of Health of the Hong Kong Government.

Twenty-four female Sprague-Dawley (SD) rats with the age of 12 week provided by the Laboratory Animal Unit were employed in this research. The average weight of each rat was approximately 300 g. And the surgical site was selected as the lateral epicondyle. Three groups were set in this study: each rat was implanted with half of a PCL 3D-scaffold (2.5 mm in length) and half of a composite (T-Mild, T-Moderate or T-Strong) 3D-scaffold (2.5 mm in length) within the bone defect. And a very tiny fragment of titanium was put between the PCL and composite scaffolds to distinguish the interface of those two segments (Fig. S1). In order to monitor the *in vivo* bone formation inside and around the implant sites, a serial time points i.e. zero, two, four, and eight weeks were set for micro-computed tomography (μ-CT) scanning.

The rat was anaesthetized, shaved and followed by decortication during the surgery. Then, a minimally invasive method was employed to create a 2-mm-diameter hole through the lateral epicondyle (≈5 mm in length) using a hand drill. The scaffolds were subsequently implanted into the defect site made on the right femur. In the end, wound was sutured layer by layer with a proper dressing applied over the incision.

2.9.2. The evaluation of new bone formation by micro-computed tomography

To evaluate the new bone formation around and inside the implant site as well as to monitor the healing process, the rats were scanned by a μ-CT instrument (SKYSCAN 1076, Skyscan Company) at each time point (zero, two, four, and eight weeks). A NRecon program (Skyscan Company) was first used to reconstruct a 2D planes. And CTAn program (Skyscan Company) was then employed to analyze new bone growth by densitometry and morphometry.

2.9.3. Histological analysis

Four- and eight-weeks post-operation, the right femurs of the euthanized rats underwent hard tissue processing and paraffin embedding. For the hard tissue processing, the standard step was performed after the femur was fixed in 10% neutral buffered formalin for 72 h. In short, a dehydrating process in an increasing concentration series of ethanol was first employed (70%, 95%, 100% × 2, each one immersed for three days). And xylene was then adopted for a three-day immersion being a transition between the 100% ethanol and methyl methacrylate (MMA, MERCK, Germany). After immersion in xylene, the specimen was treated with three stages of different MMA (i.e., MMA I, II, and III, changed every four days). The MMA I is the absolute methyl methacrylate. The MMA II and MMA III are composed of 200 mL of MMA with 0 or 50 mL butylmethacrylate (Sigma-Aldrich, USA) and 4 or 8 g of benzoyl peroxide (MERCK, Germany), respectively. After being immersed in the MMA III, the specimen was put into a 37 °C oven for more than one week to polymerize the MMA. The embedded specimen was

then cut into sections and micro-grinding down to around 50 μm thickness. For the paraffin embedding, the decalcified sample was sectioned at a 5 μm thickness and placed on adhesion slides (Thermo, USA). Finally, the sectioned specimens were stained via Giemsa, tartrate-resistant acid phosphatase (TRAP)/methyl green or Safranin O/Fast Green staining, and a light microscope was used to perform the histological analyses. Immunofluorescence staining was conducted to further confirm the type of bone formation with the use of type II collagen (Servicebio, China) antibody.

2.10. Statistical analysis

The *in vitro* experiments were conducted in triplicate. The *in vitro* and *in vivo* experimental data were analyzed by a one-way analysis of variance and expressed as means standard deviations. A p value < 0.05 was considered to be statistically significant.

3. Results

3.1. Effect of the magnesium ion on cell adhesion, migration and proliferation

3.1.1. Cell adhesion

To observe the early-stage cell adhesion behaviors in mediums with different concentrations of Mg^{2+}, time-lapse microscopic observation was conducted (Fig. S2). One-hour post-seeding with medium supplemented with magnesium ions (100, 200, and 400 ppm i.e. 4.11-, 8.22- and 16.44-mM groups), a considerable number of cells adhered to the substrate surface with some showing protrusions at their periphery, while the vast majority of the cells in 0 and 20 ppm groups were still round-shaped. After 2 h post-seeding, the cells in the 100, 200 and 400 ppm groups revealed increased cell volume as well as additional protrusions. At the same time, only a few cells in the 20-ppm group adhered onto the substrate surface, and most of the cells in the 0-ppm group still presented a spherical shape. After 4 h of culturing, some cells started to adhere onto the surface in the magnesium-free (0 ppm) medium. Compared to the 20-ppm group, cells exhibited larger and more elongated morphologies with additional magnesium ions in the medium. Finally, when the culture time reached at 6 h, all of the cells had adhered onto the substrate surfaces in the 0 and 20 ppm groups. However, in comparison, the 100, 200, and 400 ppm groups showed even more protrusions as well as flattened membranes.

After the time-lapse microscope observations, the early-stage cell adhesion behaviors of the MC3T3-E1 pre-osteoblast cells cultured in medium containing different concentrations of Mg^{2+} were further assessed via double fluorescent staining (Fig. 1a). Different cell morphologies could be viewed on the 100, 200 and 400 ppm group surfaces compared with the 0 and 20 ppm groups just after culturing for 1 h. The round-shape cells in the 0 and 20 ppm groups indicated weak adhesion of the cells to the substrates while 100, 200, and 400 ppm medium groups displayed accelerated cell-substratum adhesion, and the cells exhibited larger and polygonal morphologies in those groups. Six hours post-seeding, further expanded cell volume as well as elongated cell structures could be observed in the higher Mg^{2+} ion concentration groups. Meanwhile, smaller cells with fewer protrusions at their periphery were viewed in the 0 and 20 ppm groups.

3.1.2. Cell migration

To monitor the cell mobility in mediums with different concentrations of magnesium ions, computer-aided cell migration path-tracking as well as the following quantitative analysis were taken (Fig. 1b and c). Cells were placed at the original point at time zero and showed random distribution of trajectories in all groups. In the absence of magnesium, little persistent movement could be observed in 0 ppm group (mean cell speed = 1.42 ± 0.45 μm/unit time). Though cells in the 20 ppm group became more active, the mean cell speed of those cells was still comparatively slow (2.19 ± 0.56 μm/unit time). When the medium contained 100 ppm of Mg^{2+}, the cells exhibited the highest speed, which was significantly higher than all the other groups (6.15 ± 1.51 μm/unit time). With further increases in the Mg^{2+} concentration, the corresponding values decreased to 3.74 ± 1.43 μm/unit time with 200 ppm of Mg^{2+} and to 2.75 ± 0.77 μm/unit time with 400 ppm of Mg^{2+}.

3.1.3. Cell proliferation

Cell proliferation was evaluated by calculating the fold change in the incorporation of BrdU in mediums containing different concentrations of Mg^{2+} for 12, 24, and 72 h (Fig. 1d). Twelve hours post-seeding of the cells, no significant differences were found between any groups; however, the 100, 200, and 400 ppm groups showed higher cell proliferation properties than the 0 and 20 ppm groups. After the cells were seeded for 24 h, the 20, 100, and 200 ppm groups exhibited significantly higher values of BrdU incorporation compared to the 0 and 400 ppm groups. At 72 h, the 20 and 200 ppm groups showed significantly higher cell proliferation properties than the 0 ppm group, while the 100 ppm group was significantly higher than both the 0 and 400 ppm groups.

3.2. Characterizations of the nano magnesium oxide and composite materials

3.2.1. Characterizations of surface treated nano magnesium oxide

The TEM observation along with the SAED pattern test were taken to confirm the structure of the nanoparticles before the following experiments (Fig. 2b). The d-spacing value of the particle match well with the magnesium oxide standard JCPDS FILE (30–0794) with clear crystallinity as supported by SAED.

The molecular structure of MgO after surface treatment were confirmed by FT-IR and Raman spectroscopy with the wavenumber or Raman frequency from 450 cm^{-1} to 4000 cm^{-1} (Fig. 2c and d). The peak at 1641 cm^{-1} shows in Raman spectrum of the T-MgO is attributed to vibration peak of C═C while 2920 cm^{-1} can be attributed to vibration peak of –CH2-. Observed from FT-IR spectrum of the T-MgO, appearance of the absorption bands around 2930 cm^{-1} (C–H stretching vibration), 1703 cm^{-1} (C═O stretching vibration), 1637 cm^{-1} (C═C stretching vibration), 1177 cm-1 (ester group) and 1012 cm^{-1} (Si–O–C stretching vibration) corresponding to the characteristic of bands from the TMSPM. The results of FT-IR and Raman spectroscopy indicated that the surface treatment of the MgO by TMSPM was successful.

3.2.2. Characterizations of the composites

Based on the cellular results obtained above, to provide gradient Mg^{2+} microenvironments, composite materials which can provide mild, moderate or excess magnesium ions were fabricated by using surface-treated MgO and biodegradable polymer PCL. After the fabrication of the PCL/T-MgO composites via the solution blending process, the structure of the PCL and the selected T-Strong composite were characterized by the FT-IR method (Fig. 2d). Because the IR absorption intensity of the inorganic materials are weaker than the polymers, therefore, only the characteristic peak around 540 cm^{-1} (Mg–O stretching vibration) from the MgO can be clearly observed in the FT-IR spectra of the composites. Other parts of the FT-IR spectra are almost identical to the pure PCL.

The cross-section morphologies and magnesium distribution of all the composites with the magnification of 2000 were then observed by SEM and EDS (Fig. 2f). No matter how many MgO are incorporated, all the composites exhibited heterogeneous magnesium element distribution without large agglomerates. And with the increase of MgO into the matrix, the detected elementary intensity via EDS increased.

Fig. 2e shows the compressive moduli of the PCL and PCL/T-MgO composites. The compressive modulus of the pure PCL is 235.3 ± 7.1 MPa, which is almost 50 MPa lower than the PCL/T-MgO

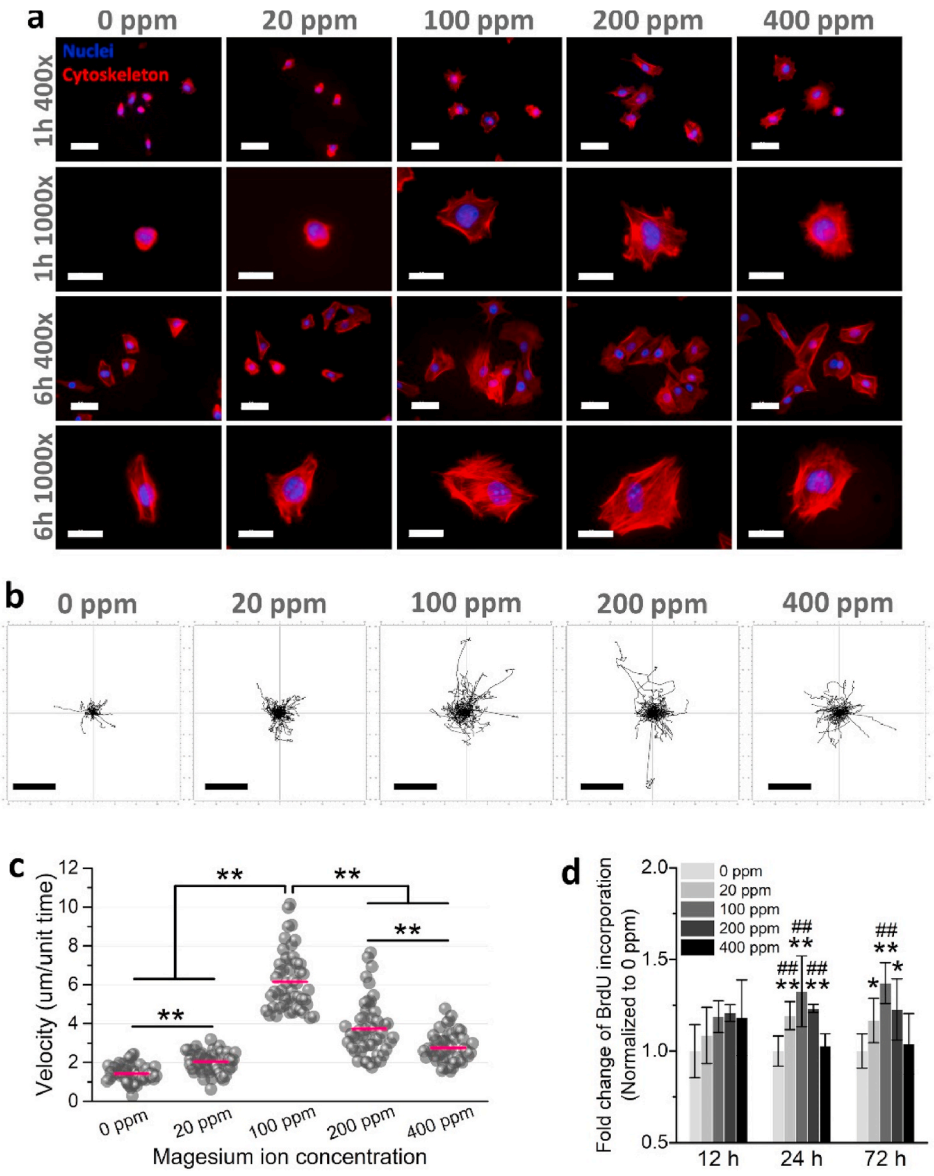

Fig. 1. Effect of different magnesium ion concentration on cell adhesion, migration, and proliferation. (a) Fluorescent staining observation of the MC3T3-E1 after culturing for one and 6 h in DMEM with different concentration of Mg^{2+}. Mediums with the magnesium ion concentrations of 100, 200, and 400 ppm accelerated cell-substratum adhesion, and cells in those groups exhibited larger and polygonal cell morphologies, while the 0 and 20 ppm groups displayed delayed cell-substratum adhesion. Scale bar 1st & 3rd row: 50 μm, 2nd & 4th row: 25 μm. (b) Computer-aided cell migration path tracking and (c) quantification of cell migration velocity. The slowest rates were seen for the 0 and 20 ppm groups. The rate peaked at 100 ppm and decreased again for the 200 and 400 ppm groups. Scale bar: 100 μm, $^{**}p < 0.01$. (d) Cell proliferation evaluated by the fold change in the incorporation of BrdU in mediums containing different concentration of Mg^{2+} for 12, 24 and 72 h. The fold change was calculated by dividing the absorbance values of the samples by those of the 0 ppm group. Statistical significance is indicated by $^{*}p < 0.05$, $^{**}p < 0.01$ vs 0 ppm; $\#p < 0.05$, $\#\#p < 0.01$ vs 400 ppm.

composite with the minimum proportion of MgO. The compressive moduli of the PCL/T-MgO composites ranged from 283.9 ± 9.7 MPa to 607.2 ± 31.9 MPa which are all in the range of human cancellous bone. It is also worth mentioning that all the differences of the compressive moduli between the PCL and PCL/T-MgO composites are significant ($p < 0.01$).

3.2.3. Ion-releasing profile of the composites

The accumulative magnesium ion concentrations of the composites immersed in SBF for 1, 3, 7, 15 and 30 days and their corresponding linear regression equations were shown in Fig. S3. The release rate of all the composites increased steadily from 37 to 48 ppm at day 1 of immersion to 228–806 ppm after 30 days, respectively. With the proportionately grow of the MgO into the polymer matrix, the release rates of the composites increase accordingly. The corresponding regression equations are approximately linear with the coefficient of determination from 0.8635 to 0.9937.

The accumulative magnesium ion concentrations of the composites immersed in DMEM for 1, 2, 4, 8, 12, 24, and 48 h were also measured (Fig. 3a). Similar to the release patterns shown in PBS solution, with a growing percentage of MgO in the polymer matrix, the release rate of the composites also increased accordingly in the DMEM. The steady release of Mg^{2+} from the composites started with 25–45 ppm at 1 h of immersion and rose to 80–380 ppm after 48 h.

3.2.4. In vitro characterizations of the composites

3.2.4.1. Cell proliferation and viabilities on composites. The BrdU assay was also used to investigate the cell proliferation property of the mouse pre-osteoblast cells exhibited on the PCL and the composites. Fig. 3b shows the cell proliferation evaluated by the fold change of the incorporation of the BrdU on samples for 1 and 3 days. As can be seen from the figure, although the composites had relatively high values, the MC3T3-E1 proliferation level on the different materials exhibited no significant differences after one day of incubation. After the cells were seeded for three days, the T-Moderate group showed a significantly higher cell proliferation level compared to the pure PCL, while the T-Mild and T-Strong groups still showed no significant differences. Fig. 4b shows the cell viability results of the PCL and composites to the MSCs measuring by the CCK-8 assay. Both one- and three-days post seeding the cells, significantly higher cell viabilities could be observed on the materials with additional magnesium element.

3.2.4.2. Morphological observation of MSCs on composites. After one day

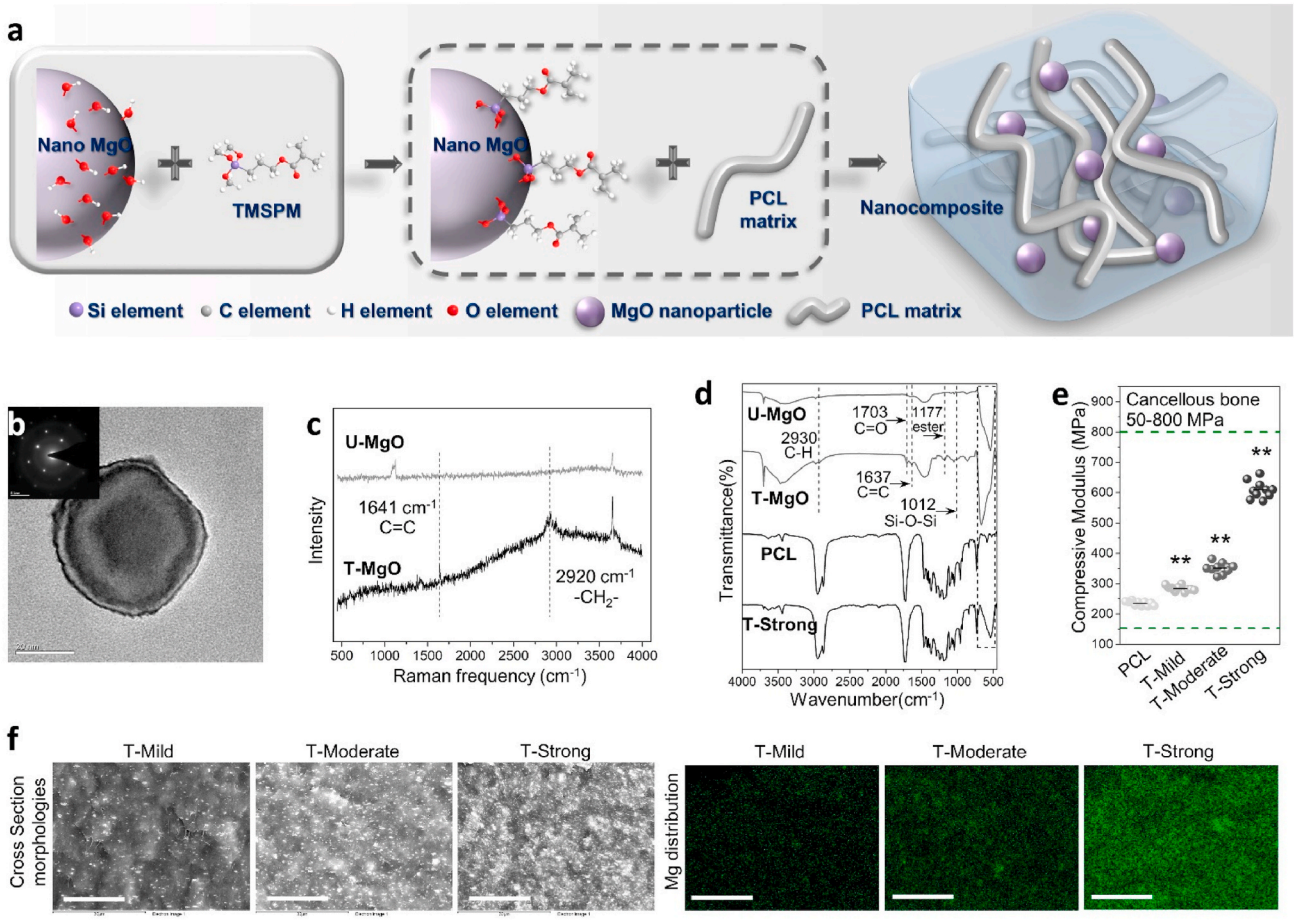

Fig. 2. Preparation and characterization of surface-treated MgO nanoparticle and magnesium enriched composites. (a) Preparation process of PCL/T-MgO composite. After the surface treatment of the MgO by 3-(Trimethoxysilyl)propyl methacrylate coupling agent, PCL/T-MgO composites were fabricated via a solution blending process with the PCL and T-MgO. (b) Transmission electron microscope observation and selected area electron diffraction pattern of the MgO nanoparticle. Scale bar: 20 nm. (c) Raman spectra of U–MgO and T-MgO. (d) FT-IR spectra of U–MgO, T-MgO, PCL and T-Strong. The Mg–O stretching vibration peak around 540 cm^{-1} from the MgO can be clearly observed in the FT-IR spectra of the composite reveals the successful preparation of the composites. (e) Compressive moduli of the PCL and PCL/T-MgO composites (**$p < 0.01$, vs PCL). Ten rod-shape specimens in each group with the diameter of 3 mm and length of 6 mm were measured with the testing speed of 1 mm/min. (f) Cross Section morphologies (upper row) and magnesium distribution (lower row) of the T-Mild, T-Moderate and T-Strong composites. Scale bar: 20 μm.

of culturing, the cellular morphology of MSCs on different materials was observed using SEM (Fig. 4a). Cells exhibited weaker adhesion with fewer protrusions showed on the PCL. Larger and much more elongated cells with considerable number of filopodia and lamellipodia exhibited on the materials encapsulated with MgO.

3.2.4.3. Osteogenic differentiation. To evaluate the osteogenic property of the PCL and PCL/T-MgO composites to MC3T3-E1 pre-osteoblasts and MSCs, the ALP assay was conducted. The results of the ALP activities are shown in Figs. 3c and 4d. For the pre-osteoblast, on day 3, significantly higher values are found on T-Mild and T-Moderate when compared to the PCL group. Whereas T-Strong group shows an ALP activity with the value of 50.1 U/mg protein which is significantly lower than the pure PCL group with the ALP activity of 101.4 U/mg protein. On day 7, though the specific ALP activities of all the groups increased dramatically, the general trend is the same with day 3, i.e. with the values of 687.1 U/mg protein and 713.2 U/mg protein, T-Mild and T-Moderate groups are significantly higher than those of the PCL which with the specific ALP activity of 426.9 U/mg protein. At the same time, the specific ALP activity of the T-Strong group is 131.1 U/mg protein. On day 14, the specific ALP activities of the PCL, T-Mild, T-Moderate and T-Strong all come down. It turns out to be that all the composite groups are significantly different with the pure PCL group. Apart from the T-Strong with the ALP activities of 64.9 U/mg protein, the composite groups with less MgO incorporated into the polymer matrix show statistically significant enhancement of specific ALP activities when compared with the PCL group. Similar to the results of the pre-osteoblast, MSCs also showed significantly enhanced ALP activities on the T-Mild and T-Moderate through the entire period tested, while lower values were noted on the T-Strong samples compared with the PCL group. The ALP staining results also demonstrated a same trend, that area positive for the ALP histochemical staining were higher on the T-Mild and T-Moderate (Fig. 4c).

3.2.4.4. Cell mineralization. The mineralization properties of the MC3T3-E1 pre-osteoblast cells and MSCs cultured on different materials for 14, 17 and 21 days were observed via ARS staining. Qualitative and quantitative results of the deposited minerals were determined and are shown in Fig. 3d, e, 4e and 4f. The positive red stains suggest the differentiation of pre-osteoblasts and MSCs into mature osteoblasts with the calcium deposition. For the pre-osteoblasts, the onset of mineralization on the T-Mild occurred between day 14 and day 17 while only a few calcium nodules formed on the PCL and the T-Strong at day 21. Besides that, a considerable number of mineralized bone nodules formed on T-Moderate prior to

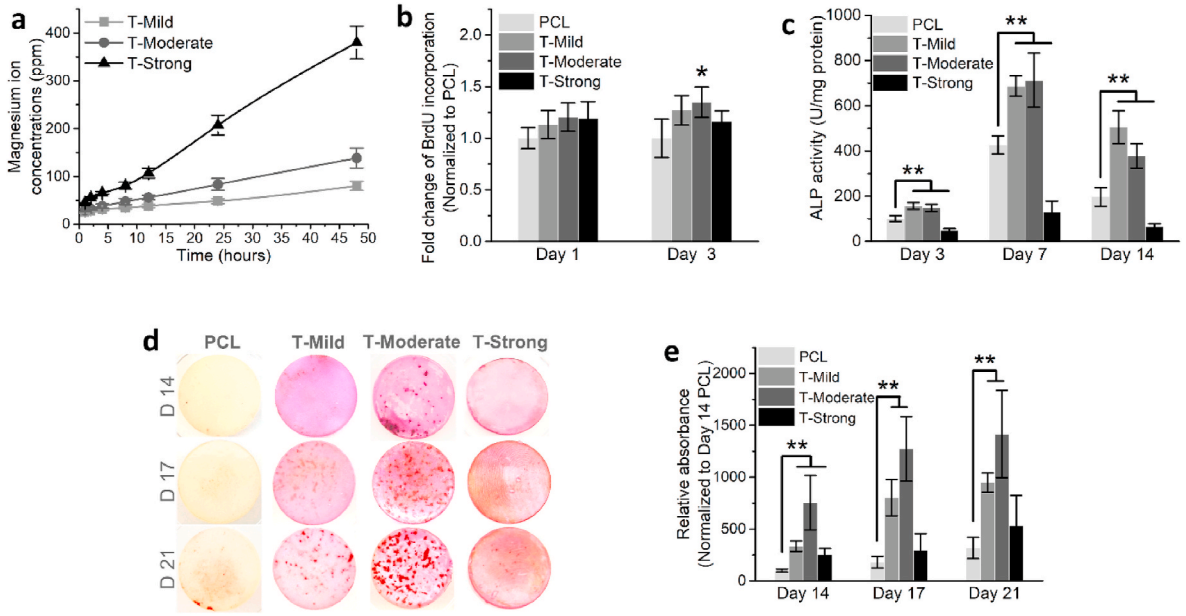

Fig. 3. *In vitro* characterization of pre-osteoblast on magnesium enriched composites. (a) Accumulative magnesium ion concentrations of the composites immersed in DMEM medium for 1, 2, 4, 8, 12, 24, and 48 h. (b) Cell proliferation evaluated by the fold change of the incorporation of BrdU on different samples for 1 and 3 days. The fold change was calculated by dividing the absorbance values of the samples to the PCL. Statistical significance is indicated by * $p < 0.05$ compared to the PCL control. (c) ALP activities of MC3T3-E1 pre-osteoblasts cultured with the osteogenic induction medium on PCL, T-Mild, T-Moderate and T-Strong for 3, 7 and 14 days. Significantly higher (**$p < 0.01$ vs PCL) specific ALP activities were found on the T-Mild and T-Moderate as compared to the PCL. (d) and (e) Alizarin red S (ARS) staining of MC3T3-E1 on PCL, T-Mild, T-Moderate and T-Strong to verify the mineralization properties. (d) ARS staining was carried out after the MC3T3-E1 was cultured for 14, 17 and 21 days with the osteogenic induction medium on different materials. (e) At each time point, the ARS stain was dissolved in 10% acetic acid and the absorbance of the extracts was measured by a multimode detector at 450 nm wavelength. To obtain the relatively absorbance, the results were normalized to the day 14 PCL, **$p < 0.01$ vs PCL. (For interpretation of the references to color in this figure legend, the reader is referred to the Web version of this article.)

day 14. Day 14 onwards, a remarkable increase of the calcium deposition on T-Moderate surface can be observed in the following three days. Although the increase of the calcium deposition can be noted on the T-Mild, the increase rate is fairly slower than that observed on T-Moderate. At each time point, the individual calcium nodule formed on the T-Moderate are also much larger compared to other samples. Furthermore, the T-Moderate group shows the highest quantitative results during the entire period of the assay. It is up to 7.5-fold, 2-fold and 3-fold higher than the PCL, T-Mild and T-Strong groups on day 14, respectively. With the time goes on, T-Strong group shows limited growth of the relative absorbances which are just barely higher than the PCL group. For the MSCs, similar phenomena and results were also observed and detected on all the specimens (Fig. 4e and f).

3.3. Local magnesium ionic microenvironment in osteoblastic activities

3.3.1. Cell morphology observation

To investigate the effect of the magnesium microenvironment on osteogenic cell behavior, eGFPOB were first cultured on different co-disks and the cell morphologies were observed via fluorescence microscope after a one-, two- or three-day incubation (Fig. 5b). After one day of culturing, the cells had spread well on the composite sides of the co-disks. It is also worth noting that, on composite sides, a larger and much more elongated cell morphology could be observed with an increased proportion of MgO. In sharp contrast, besides the PCL/T-Strong group, many fewer cells could be found on the PCL side as compared with composite sides, indicating that the spreading and adhesion of the cells was weaker on the PCL side. At the same time, spherical cell morphology could be seen on the PCL side in all groups. After incubation for two days, the cell number and area increased on the PCL side in all groups, while the cells exhibited even better spreading on the composite sides. A gradient increase in cell density and better cell morphologies were seen on PCL side with the increased percentage of MgO in the corresponding composite side. On day three, the cells revealed good spreading and nearly grew to 100% confluence on all of the co-disks except the PCL side from the PCL/T-Mild co-disk, on which cells were still loosely adhered with a low density.

After three days of culturing, the MC3T3-E1 pre-osteoblast cell morphologies presented on different co-disks were observed using SEM (Fig. 5c). Similar to the fluorescence microscope view of the eGFPOB, the cells on PCL/T-Moderate co-disk were well-spread and had grown to 100% confluence. Though the cells didn't cover the whole area of the T-Mild surface, there was still an obviously larger cell-spreading area than on the PCL side. It is noteworthy that with the increasing ratio of MgO in the corresponding composite sides, the magnesium element intensity detected on the PCL sides also increased.

To further observe the cell morphologies as well as quantitatively analyze the cell number on each side of the co-disk, fluorescent staining was used to stain the cytoskeleton and nuclei (Fig. 5d). On the T-Mild, T-Moderate and T-Strong surfaces, the cells spread well and exhibited polygonal shapes. The cells grew to almost 100% confluence on the T-Moderate surface, though they covered a bit less area percentage on the T-Mild and T-Strong surfaces. The sharp contrast occurred between the corresponding PCL surfaces, however. The PCL surfaces of the PCL/T-Moderate and PCL/T-Strong co-disks had nearly fully coverage of cells, at the same time, very few cells can be observed on the PCL side of the PCL/T-Mild co-disk (Figs. 5d–1, -5 and -9). The cell nuclei stain presented round and well distributed nuclei spread over the surface of T-Mild, T-Moderate, T-Strong and PCL from the PCL/T-Moderate and PCL/T-Strong co-disks, while the PCL from the PCL/T-Mild co-disk showed dramatically fewer nuclei in comparison (Figs. 5d–2, -6 and -10). The qualitative results showed that on the PCL/T-Mild co-disk, over 2.5-fold more cells could be found on the T-Mild surface compared to the PCL side. Meanwhile, though slightly more (~20%) nuclei could be counted on the T-Moderate, significant differences from the PCL side

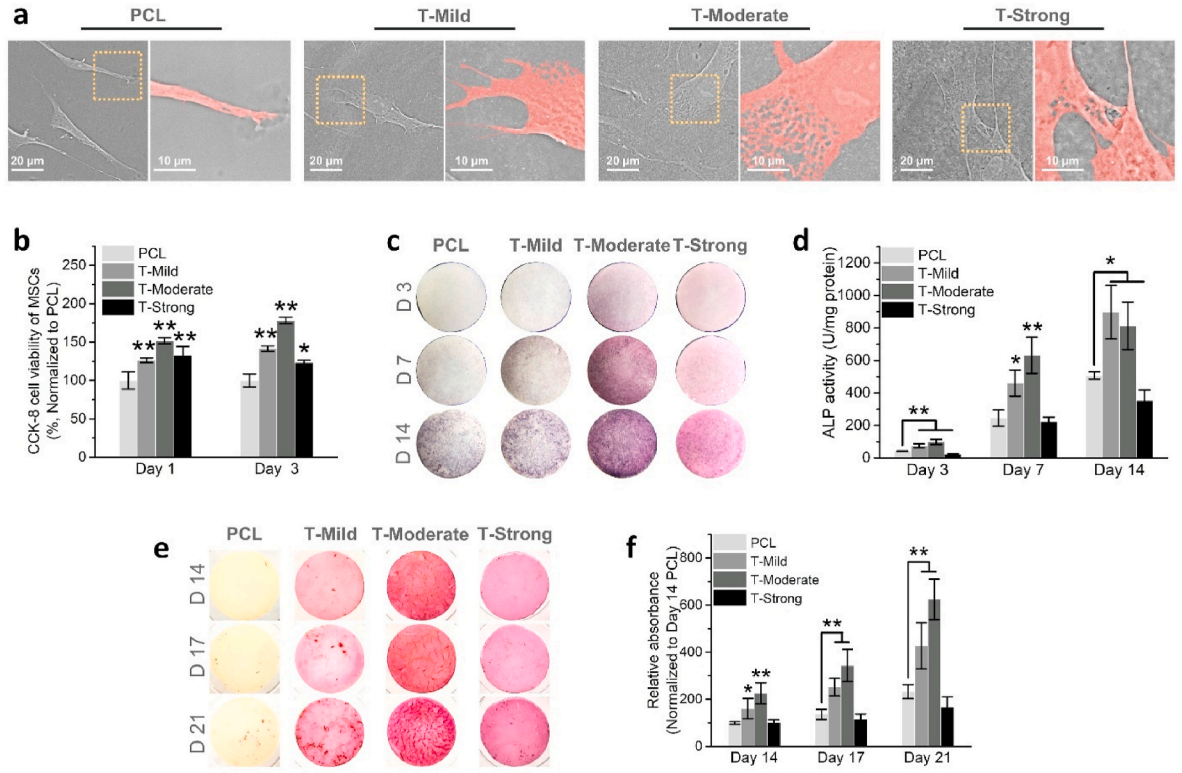

Fig. 4. *In vitro* performances of human mesenchymal stem cells on magnesium enriched composites. (a) MSC morphological observation by using SEM after 1 day of culturing on different surfaces. Scale bar: left side: 20 μm, right side: 10 μm. (b) Cell viabilities of the MSCs cultured on different samples for 1 and 3 days. The percentage cell viability was calculated by dividing the absorbance values of the samples to the PCL control. Statistical significances are indicated by * $p < 0.05$ and ** $p < 0.01$ compared to the PCL control. (c) ALP staining and (d) ALP activities of MSCs cultured with the osteogenic induction medium on PCL, T-Mild, T-Moderate and T-Strong for 3, 7 and 14 days. Statistical significances are indicated by * $p < 0.05$ and ** $p < 0.01$ compared to the PCL control. (e) and (f) Alizarin red S (ARS) staining of MSCs on PCL, T-Mild, T-Moderate and T-Strong to verify the mineralization properties. (e) ARS staining was carried out after the MSCs were cultured for 14, 17 and 21 days with the osteogenic induction medium on different materials. (f) At each time point, the ARS stain was dissolved in 10% acetic acid and the absorbance of the extracts was measured at 450 nm wavelength. To obtain the relatively absorbance, the results were normalized to the day 14 PCL, * $p < 0.05$, ** $p < 0.01$ vs PCL. (For interpretation of the references to color in this figure legend, the reader is referred to the Web version of this article.)

could not be detected on the PCL/T-Moderate co-disk. Similar situation also occurred on the PCL/T-Strong co-disk, the number of nuclei counted on both sides are almost the same (Fig. 5d 4, 8 & 12).

3.3.2. Monitoring of local spatial distribution of magnesium ions

Scanning ion-selective electrode technique (SIET) with small modifications was used to measure the net fluxes of Mg^{2+} over the surface of PCL/T-Mild, PCL/T-Moderate and PCL/Strong co-disks (Fig. 5e). All three T-Mild, T-Moderate and T-Strong showed even ion release in a narrow range from 90 to 280 pmol $cm^{-2}{\cdot}s^{-1}$ on T-Mild, 167–355 pmol $cm^{-2}{\cdot}s^{-1}$ on T-Moderate and 897–1341 pmol $cm^{-2}{\cdot}s^{-1}$ on T-Strong. Noteworthy, the PCL from the PCL/T-Mild co-disk revealed a low Mg^{2+} changing rate, within 100 pmol $cm^{-2}{\cdot}s^{-1}$ over most of the area, with some parts exhibiting below 50 pmol $cm^{-2}{\cdot}s^{-1}$ on this PCL surface. In contrast, the PCL surfaces from PCL/T-Moderate and PCL/T-Strong presented obviously higher Mg^{2+} changing rate, which ranged from 88 to 378 pmol $cm^{-2}{\cdot}s^{-1}$ and 800–1134 pmol $cm^{-2}{\cdot}s^{-1}$.

3.4. In vivo studies

3.4.1. 3D scaffold characterization

After fabricated via low-temperature extrusion-based manufacturing technique, the surface morphologies of the 3D scaffolds were then observed by digital camera and SEM. The images shown in Fig. 6a revealed that the 3D scaffolds in regular arrays have well-defined geometry as well as highly regular and interconnected pores. The width of the strands ranged from 600 to 800 μm forming the opened regular macropores of 300–400 μm in size. For the PCL/T-MgO composites, phase separation was not observed under high magnification imaging.

3.4.2. The evaluation of new bone formation by micro-computed tomography

The formation of new bone inside and around the 3D-scaffolds was examined by *in vivo* study. At each time point (zero, two, four and eight weeks), micro-computed tomography was also used to scan the rats in order to monitor the *in vivo* healing process. The cross-sectional images of the right femur with the view of the implant sites at each time point were taken to evaluate the bone formation with different scaffolds (Fig. 6b). After two weeks, barely mineral deposition can be observed from both side of the PCL/T-Mild group. In the PCL/T-Moderate group, the new bone formation started inside the T-Moderate scaffold from week two, while the PCL side showed nearly no sign of new bone formation at this time. By contrast, the PCL side showed considerably more calcium deposition in the PCL/T-Strong group two weeks after the surgery. Besides that, very limited bone formation could be observed inside the T-Strong scaffold. From week four onwards, some new bone formation could be viewed within the T-Mild scaffold and PCL scaffold from the PCL/T-Moderate group while remarkable bone healing was seen inside the T-Moderate. It is notable that the bone was marginally formed from the edge of the defect site in the T-Strong scaffold from week four to week eight. Meanwhile, the PCL scaffold from the PCL/T-Strong group revealed a dramatic amount of new bone formation in the whole area of the defect starting from four weeks post-operation. The PCL side in the PCL/T-Mild group, however, only formed restricted new bone even at the last time point.

After the evaluation of new bone formation by micro-CT

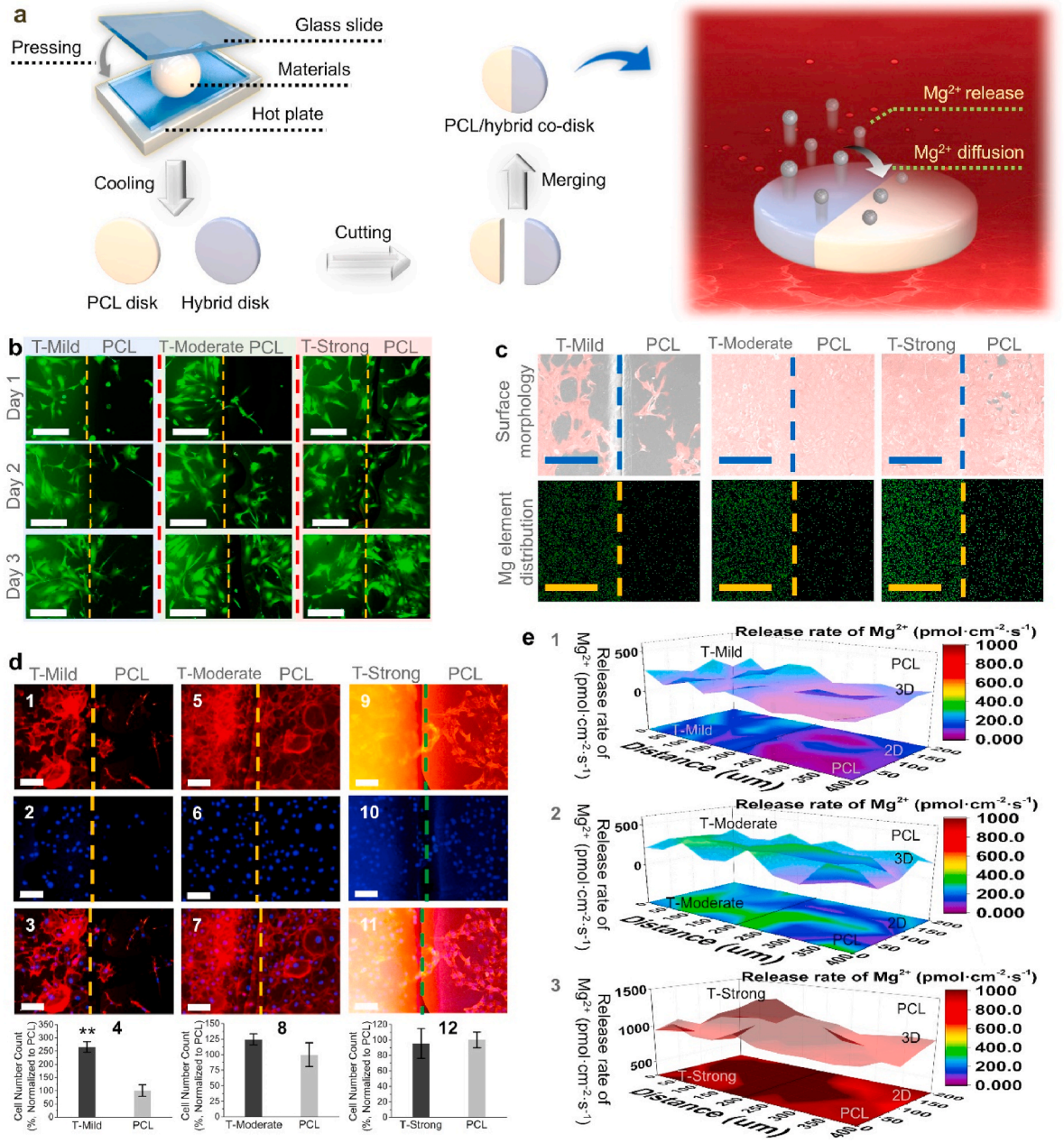

Fig. 5. Local magnesium ionic microenvironment in cellular activities. (a) Preparation process and magnesium-ion-release demonstration of the PCL/composite co-disk. (b) Microscopic views of eGFPOB cultured on different PCL/composite surfaces for one, two and three days. Cells spread well on the composite sides of the co-disks while gradient increase in cell density and better cell morphologies were seen on PCL side with the increased percentage of MgO in the corresponding composite side. Scale bar: 200 μm. (c) Magnesium element distribution and cell morphologies of MC3T3-E1 after culturing for three days on different PCL/composite surfaces. Cells on PCL/T-Moderate and PCL/T-strong co-disks were well-spread and had grown to 100% confluence. On the PCL/T-Mild co-disk, obviously larger cell-spreading area was found on the surface of T-Mild compared with PCL side. Scale bar: 200 μm. (d) MC3T3-E1 pre-osteoblast adhesion measured on the PCL/composites after incubation for three days: 1), 5) & 9) cytoskeleton in red stained with rhodamine; 2), 6) & 10) nuclei in blue stained with Hoechst33342; 3), 7) & 11) overlay image; 4), 8) & 12) number of cell on each side of co-disk (**$p < 0.01$ vs PCL side). On the PCL/T-Mild co-disk, over 2.5-fold more cells could be found on the T-Mild surface compared to the PCL side. Meanwhile, on the PCL/T-Moderate co-disk, just slightly more (~20%) nuclei could be counted on the T-Moderate compared to PCL side. Scale bar: 100 μm. (e) Magnesium ion release rate mapping over the scanned area of the (1) PCL/T-Mild and (2) PCL/T-Moderate and (3) PCL/T-Strong surfaces. (For interpretation of the references to color in this figure legend, the reader is referred to the Web version of this article.)

reconstruction images, the statistical results of the percent changes in bone volume inside the scaffolds over time were calculated (Fig. 6c). Two weeks post-implantation, T-Moderate exhibited 6.9% new bone formation, which was significantly higher than all of the other scaffolds. The PCL scaffold from the PCL/T-Strong group increased 2.8%, which also showed a significant difference from most of other implants. In the following time points, the percentage change in bone volume inside of the T-Moderate scaffold increased from 12.6% at week four to 25.5% at week eight. The PCL scaffold from the PCL/T-Strong group revealed a similar bone growth to the T-Moderate scaffold, which was also significantly higher than the T-Strong and the PCL from the PCL/T-Mild and PCL/T-Moderate groups. At the last time point, the T-Mild scaffold and PCL scaffold from the PCL/T-Moderate group both presented dramatic bone volume increase to 16.2% and 15.3%, respectively. At the same time, the PCL scaffold from the PCL/T-Strong group showed 18.7% new bone formation, which was significantly higher than the T-

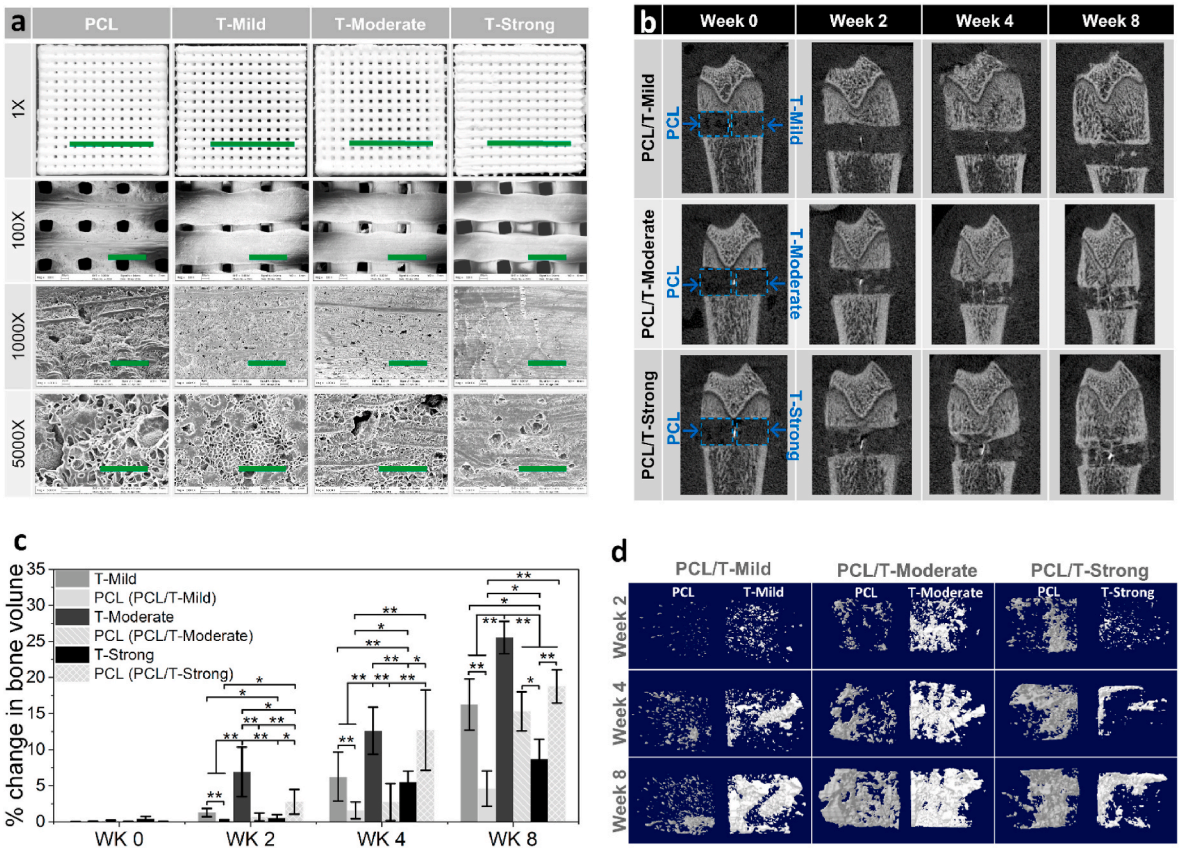

Fig. 6. Surface morphology observation and evaluation of new bone formation by micro-computed tomography. (a) Surface morphologies of the scaffolds via camera (1st row) and SEM observation (2nd -4th rows), Scale bar 1st row: 10 mm, 2nd row: 1 mm, 3rd row: 100 μm, 4th row: 25 μm. The images reveal that the 3D scaffolds in regular arrays have well-defined geometry as well as highly regular and interconnected pores. (b) Micro-CT reconstruction images of the lateral epicondyle of the newly formed bone in PCL/T-Mild, PCL/T-Moderate and PCL/T-Strong scaffolds. The PCL scaffold from the PCL/T-Strong group revealed steady increase in bone volume in the whole area of the defect starting from two weeks post-operation while merely restricted new bone formed inside the PCL scaffold from PCL/T-Moderate group as early as week four. (c) The percent changes in bone volume in PCL/T-Mild, PCL/T-Moderate and PCL/T-Strong scaffolds immediately after surgery and two, four, eight weeks post-operation (*$p < 0.05$, **$p < 0.01$). The increasing rate of bone volume grew almost linearly in the T-Moderate scaffold, which was significantly higher than the T-Mild, T-Strong as well as the PCL from PCL/T-Mild and PCL/T-Moderate throughout the whole period of the experiment. (d) 3D reconstruction models of newly formed bone within the defect sites.

Strong scaffold (8.7%). It is noticeable that from week two onward, whether higher or lower, the new bone formation of each PCL scaffold showed significant difference from the corresponding composite side.

To observe the bone formation process within the scaffolds more intuitively, 3D models of the bone defects were generated and shown in Fig. 6d. The results are consistent with the statistical analysis. At each time point, the volume of newly formed bone within the PCL scaffold is closely related to the corresponding composite scaffold. Increasing bone formation can be seen inside the PCL side when the composite side contains higher amount of MgO. And the T-Moderate always shows the largest amount of mineralized bone and delicate porous structure compared with the other two composite scaffolds.

3.4.3. Histological analysis

Four weeks and eight weeks post-implantation, Giemsa stained histological examinations were first conducted to analyze the remodeled bone tissue within the defect area (Fig. 7). The dashed black frame indicates the defect area and scaffold in the lateral epicondyle. Four weeks post-implantation, a remarkable amount of mature bone and marrow were observed surrounding the T-Moderate scaffold, while fibrous connective tissues with ordered spindle-shaped cells were present inside the defect area of the PCL scaffold from the PCL/T-Moderate group (Fig. 7b). A small amount of bone tissue was also newly formed at the sites close to the T-Moderate scaffold. In contrast, in the PCL/T-Strong group, the PCL scaffold exhibited a considerable amount of new bone formation, however, the defect region implanted with the T-Strong scaffold lacked mineralized deposits and was filled with fibrous tissue (Fig. 7c). A similar situation occurred in the PCL/T-Mild group but with the opposite result. More bone tissue could be found within the T-Mild scaffold, while fibrous tissues, along with a very limited amount of new bone, formed inside the PCL scaffold (Fig. 7a). Eight weeks post-implantation, some organized bone formed on the PCL sides near the T-Mild and T-Moderate scaffolds (Fig. 7d and e). At the same time, fibrous tissue could not be found within the defect area implanted with T-Moderate, and newly formed bone as well as a mature extracellular matrix encircled the scaffold. However, fibrous connective tissues were still shown in the T-Mild scaffold. In the PCL/T-Strong group, a small amount of mineralized bone was just generated from the edge between the T-Strong and the PCL into the inner part of the T-Strong scaffold (Fig. 7f). Meanwhile, fibrous connective tissues continued to surround the surface of the T-Strong scaffold. In sharp contrast, a progressive amount of bone and marrow were shown surrounding the PCL scaffold from the PCL/T-Strong group. Eight-week post implantation, the osteoclasts formation within the bone defect was determined by TRAP/methyl green staining (Fig. 7g). In the PCL/T-Moderate group, bone from both side of the defect had considerable number of TRAP-positive cells in the new bone area, indicating that newly formed bones were undergone remodel process. Few TRAP-positive osteoclasts were detected in the T-Mild (PCL/T-Mild) and PCL (PCL/T-Strong) implanted defect areas, while within the other side of the defect, TRAP-positive

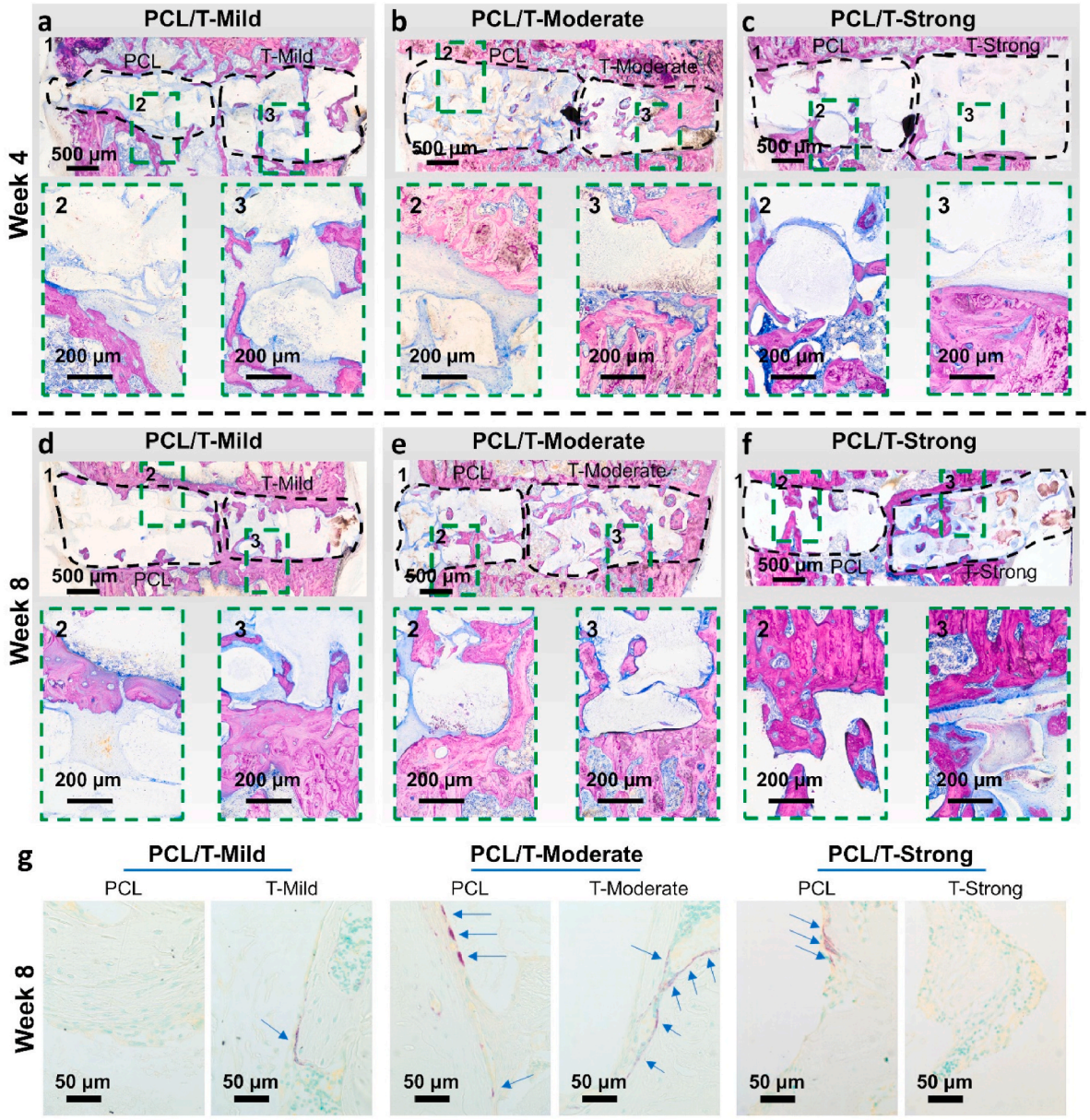

Fig. 7. Giemsa stained histological images of the bone defect sites. (a–f): 1) 40x magnification histological photograph of the defect site four- or eight-weeks post-implantation of the PCL scaffold and T-Moderate or T-Strong scaffolds with Giemsa staining. 100x magnified histological photographs showing the bone/implant interface, fibrous connective tissue, and new bone formation inside the 2) PCL scaffold and 3) T-Mild, T-Moderate or T-Strong scaffolds. (g) TRAP/methyl green stained bone tissues after eight-weeks implantation. The osteoclasts were stained in purple/red and indicated by blue arrows. (For interpretation of the references to color in this figure legend, the reader is referred to the Web version of this article.)

cells were absent.

To further investigate the type of bone formation process within the defect areas and differentiate the endochondral and intramembranous ossification, Safranin O/Fast Green and collagen II immunofluorescence staining were adopted. Fig. 8a shows the stained articular cartilage and growth plate that indicated the chondrocytes, cartilage, and typical endochondral ossification. The red or orange stain of the cartilage was observed as a precursor on which newly formed bone was laid down while cartilage staining was absence at all time points within the bone defect sites (Fig. 8b). At the same time, the ossification points appeared in the fibrous connective tissue, and osteoid was secreted within the fibrous membrane. Eight weeks post-implantation, some woven bone had formed within the T-Moderate scaffold and the PCL scaffold from the PCL/T-Strong group. The expression of type II collagen was also used to identify the bone formation process (Fig. 9). Compared with the growth plate control, no expression was observed within the defect 4- or 8-week post-operation. All this confirmed that bone formation occurred through intramembranous ossification inside the defect.

4. Discussion

It is well-known that the microenvironment plays a crucial role in cell behavior regulation, including cell-substrate adhesion, cell migration, proliferation, and differentiation, etc. [28,29]. Precisely control of the temporal and spatial cues that form a suitable microenvironment is necessary for the construction of complex functional tissues [30–32]. The magnesium ion is an important factor in cellular regulation [33]. Therefore, to further understand the influence of the Mg^{2+} microenvironment on osteogenic cellular responses, Mg^{2+}-containing culture mediums were first employed to interact with pre-osteoblast at the early stage. Cell-matrix adhesion is the first interactive step between anchorage-dependent cells and substrate materials. This adhesion is

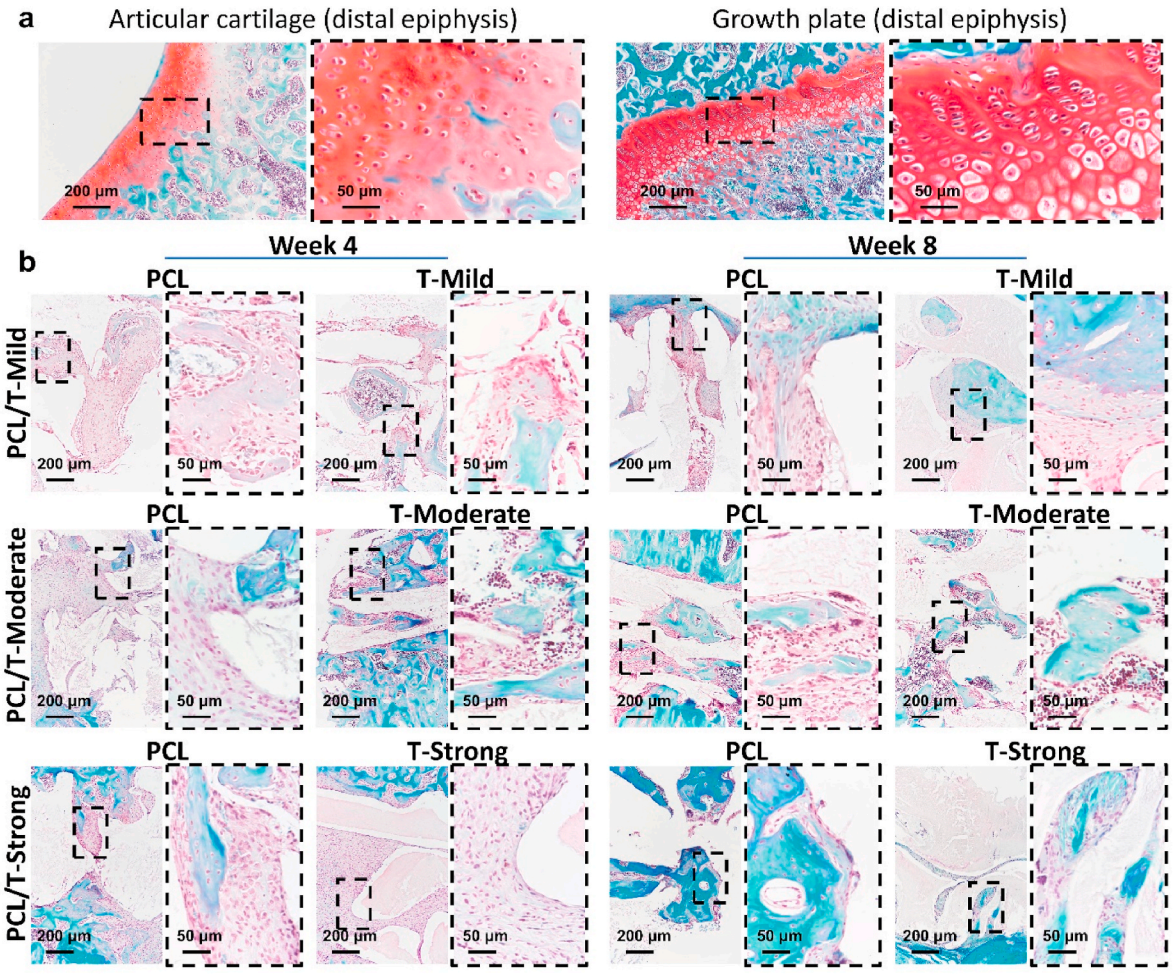

Fig. 8. Endochondral and intramembranous ossification identified by Safranin O/Fast Green staining. (a) Safranin O/Fast Green stained histological images of the articular cartilage and growth plate from the harvested bone tissue showed chondrocytes, cartilage, and endochondral ossification. (b) Safranin O/Fast Green stained histological images of the defect sites. Within each defect, cartilage staining (orange or red) was absent at all time points, while the ossification centers and osteoid appeared in the fibrous connective tissue membrane. (For interpretation of the references to color in this figure legend, the reader is referred to the Web version of this article.)

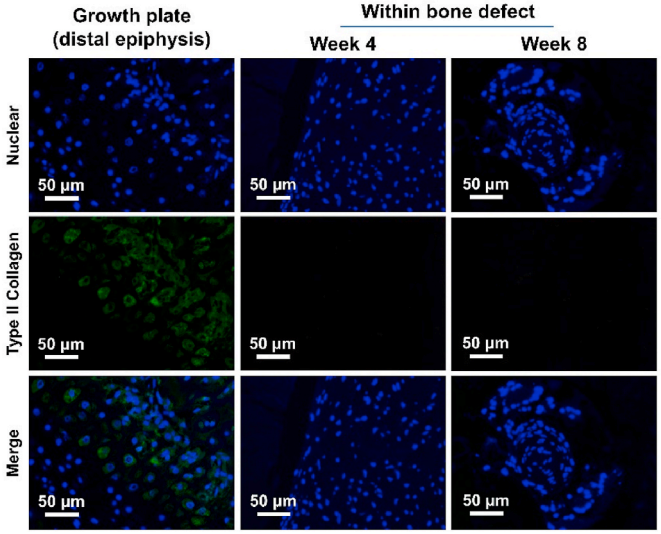

Fig. 9. Immunofluorescence staining of type II collagen within the bone defect after 4- or 8-week implantation. Compared with the growth plate control, no expression of the collagen II was observed within the defect. This further confirmed that the bone formation occurred through the intramembranous ossification process with this defect model.

essential for cell survival, migration, cell cycle progression, differentiation, and even tissue organization, due to its importance in combinations individual cells into tissues [34,35]. In this study, time-lapse microscopy was conducted, and fluorescent staining observations were made to demonstrate early-stage cell adhesion behaviors in mediums treated with different concentrations of Mg^{2+} (Fig. S2 and Fig. 1a). With the additional magnesium in the normal medium, the cells exhibited larger and much more elongated morphologies at very early stages, which indicated better substrate-cell adhesion in this phase. Previous studies have also shown that Mg-incorporated titanium oxide surfaces increase cellular attachment significantly compared with untreated surfaces [36]. Transmembrane receptor integrins on the cell membrane are essential for regulating substrate-cell adhesion of osteoblast cells [37]. Several publications have revealed that Mg^{2+} enhances the connection of integrins more so than Ca^{2+} [38,39]. Primary adhesion of cells can therefore be facilitated by increased extracellular magnesium levels [40,41] and this is supported by our findings here.

The migratory ability that results from various chemical and stepwise mechanical interactions between the extracellular microenvironment and cells themselves determines the positioning and assembly of these cells for the construction, rebuilding, protection and repair of multi-cellular organisms [42,43]. Since it plays a crucial role in colonization, cell migration is very important for applications such as tissue engineering, for instance Ref. [44]. To monitor the cell mobility

presented in various mediums containing different concentrations of magnesium ions, qualitative observation and quantitative velocity analyses were conducted in this study (Fig. 1b and c). Though all the groups containing additional Mg^{2+} exhibited better substrate-cell adhesion at early stages compared to the normal and Mg^{2+}-deficient groups, the mobility of MC3T3-E1 pre-osteoblast cells peaked at 100 ppm and dropped again with increased Mg^{2+} concentration. A previous study indicated that suitable extracellular Mg^{2+} density is essential for platelet-derived growth factor (PDGF)-induced human osteoblast-like MG-63 cell migration and proliferation [45]. PDGF up-regulates the melastatin-like transient receptor potential 7 (TRPM7) channel to ensure long-term Mg^{2+} homeostasis in osteoblastic cells, which promotes migration and proliferation of the osteoblasts. The study also demonstrated that the migration and proliferation of osteoblastic cells stimulated by PDGF were significantly reduced with low extracellular Mg^{2+} density. This was in accordance with our data, which indicated that a magnesium-deficient environment results in significantly lower cell mobility. Accumulating evidence has revealed that extracellular magnesium and calcium ion levels obviously affect the migratory and adhesive activities of multiple cell types [46,47]. A high magnesium level also potentiates human umbilical vein endothelial cellular migration in response to angiogenic factors [48]. Because magnesium is a cofactor of cyclic adenosine monophosphate (cAMP)-dependent phosphodiesterase and adenylate cyclase, sensitization to motogenic factors may be dependent on the fact that raised magnesium concentrations could alter cAMP, which regulates endothelial migration [49,50]. It is also important to note that magnesium is essential for myosin ATPase activity and the assembly of actin, which are two crucial elements of the motor responsible for cell migration [48]. Nevertheless, the results reported herein indicate that an appropriate concentration of Mg^{2+} should be taken into consideration when it is used to regulate cell migration.

Sufficient osteoblast proliferation is indispensable in both the formation of bony tissue and the regulation of bone resorption; thus, it aids in maintaining equilibrium in the bone remodeling process [45]. In the current study, the cell proliferation properties presented in the mediums containing different concentrations of Mg^{2+} were determined by the fold change of the incorporation of BrdU for 12, 24, and 72 h (Fig. 1d). Like the cell mobility results, the proliferation properties of the pre-osteoblast cells peaked at 100 ppm after 24 h of culturing, and the magnesium-deficient group always exhibited the lowest values. Compelling evidence has revealed that magnesium content is directly associated with proliferation in normal cells since it stimulates the synthesis of DNA and proteins [33,51]. Some data has also demonstrated that upon mitogenic stimuli, cells are able to raise their intracellular magnesium content, probably through magnesium influx cativation [52,53]. In turn, magnesium deficiency induces inhibition of the synthesis of proteins and DNA, thereby resulting in growth arrest [54,55]. From the mechanistic viewpoint, magnesium deficiency might affect cell cycle control via up-regulation of the cyclin inhibitor $p27^{Kip1}$, which then influences cyclin E-dependent kinases [56,57]. However, strong inhibition would also occur in cells cultured at higher-than-optimal Mg^{2+} concentrations [58]. In terms of MC3T3-E1 pre-osteoblast cells, the optimal Mg^{2+} concentration should be around 100 ppm (4.11 mM). With the controlled local magnesium ionic microenvironment, cell adhesion, migration and proliferation can be all upgraded, thus leading to an accelerated bone healing.

To create a specific magnesium ionic microenvironment using biomaterials, a series of composites containing gradient proportions of surface-treated nano-MgO and PCL were fabricated. The preparation of the inorganic/organic nanocomposites, however, was also demonstrated as a challenge in a lot of researches due to difficult dispersion of nanoparticles into polymer matrices. In order to achieve homogenous distribution of the nano-MgO in the polymer matrices, it is necessary to make the nano-MgO chemically similar to the matrix material via surface modification. Silane coupling agents are a class of compounds which contain two kinds of functional groups in their molecular structure. These functional groups give them the potential to play roles as intermediary to bond with both organic (polymer matrix) and inorganic (nano-MgO) phases [59,60]. The silane coupling agent TMSPM was then used to treat the nano-MgO. Trimethoxysilyl group (-Si$(OCH_3)_3$ group) from one side of the TMPSM monomer molecule can form strong chemical bonds with the inorganic phase by condensation reaction while methacryloxy group from the other side of the monomer molecule can make it more compatible to the polymer matrix because of the similarity and intermiscibility of solubility parameters as well as the similarity and intermiscibility of hydrogen bonds [61,62]. The FT-IR and Raman spectroscopy results (Fig. 2c & d) confirmed the successful preparation of surface modified MgO. Finally, the surface treatment of the MgO efficaciously prevented the aggregation of the nanoparticles, hence obtaining a homogeneous MgO distribution as well as a remarkable interface quality with the polymer (Fig. 2f). The homogeneous distribution of the T-MgO can further yield enhanced mechanical properties. No matter how many MgO were incorporated, the compressive modulus of each composite was significantly higher than the pure PCL (Fig. 2e) and all were in the range of human cancellous bone. The effect of matrix elasticity and stiffness on stem cell lineage specification has been extensively investigated in MSCs. MSCs cultured on soft matrices that mimic brain (0.1–1 kPa) obtain a neural phenotype, while cells cultured on stiffer matrices that mimic bone (25–40 kPa) or muscle (8–17 kPa) differentiate toward osteogenic or myogenic lineages, respectively [63].

After verification of the accumulative Mg^{2+} release profiles of all the composites (Figs. S3 and 2a), Cellular morphological observation, BrdU cell proliferation and CCK-8 cell viability assays (Figs. 3b, 4a and 4b) were carried out. The cell proliferation property peaked on the composite with moderate Mg^{2+} release. Studies have shown that Mg-incorporated biomaterial surfaces could increase cellular attachment [64,65]. Our previous studies have also found an optimal range of Mg^{2+} levels, which could upregulate cell viability and proliferation of human osteoblasts (SaOS-2) and mouse pre-osteoblasts (MC3T3-E1) [66–68]. Accordingly, the T-Moderate should be the most appropriate composite with the above data. ALP staining and ALP activity assays were then conducted to evaluate the osteoinductivity of all the materials to MC3T3-E1 pre-osteoblasts (Fig. 3c) and human MSCs (Fig. 4c and d). Statistically significant enhancement of specific ALP activities were indicated in the T-Mild and T-Moderate groups compared to the PCL group, whereas the T-Strong group was significantly lower than the PCL group throughout the entire experimental period. It has been reported that high levels of magnesium ions can impair osteoblast activities (e.g., differentiation and mineralization properties) [69]. Our results indicated that the Mg^{2+} released from the T-Mild and T-Moderate groups was likely within the appropriate range for Mg^{2+} levels, while T-Strong group was not. ECM mineralization is the eventual phenotypical expression of osteoblast differentiation [70]. The qualitative and quantitative results of the cell mineralization properties of the different materials in this study also revealed that with higher calcium deposition on the surface, T-Moderate should have the most potential to stimulate bone growth *in vivo*, whereas T-Mild and T-Strong should provide an Mg^{2+}-deficient and excess microenvironments, respectively.

To further understand the cell behaviors present within different magnesium ionic microenvironments offered by magnesium oxide-loaded composites, PCL/composite co-disks were employed to observe cell morphologies. The fluorescence microscopy experiments using eGFPOB cells (Fig. 5b) revealed that even a micron-scale magnesium-ionic microenvironment can certainly affect osteogenic cell behaviors. Though the PCL and the composites were spliced together without a gap, the cells exhibited different morphologies and responses on each side of every co-disk. Many studies have also demonstrated that micron-scale or nano-scale microenvironments, such as r biochemical, topography, or mechanical cues, could play important roles in cellular

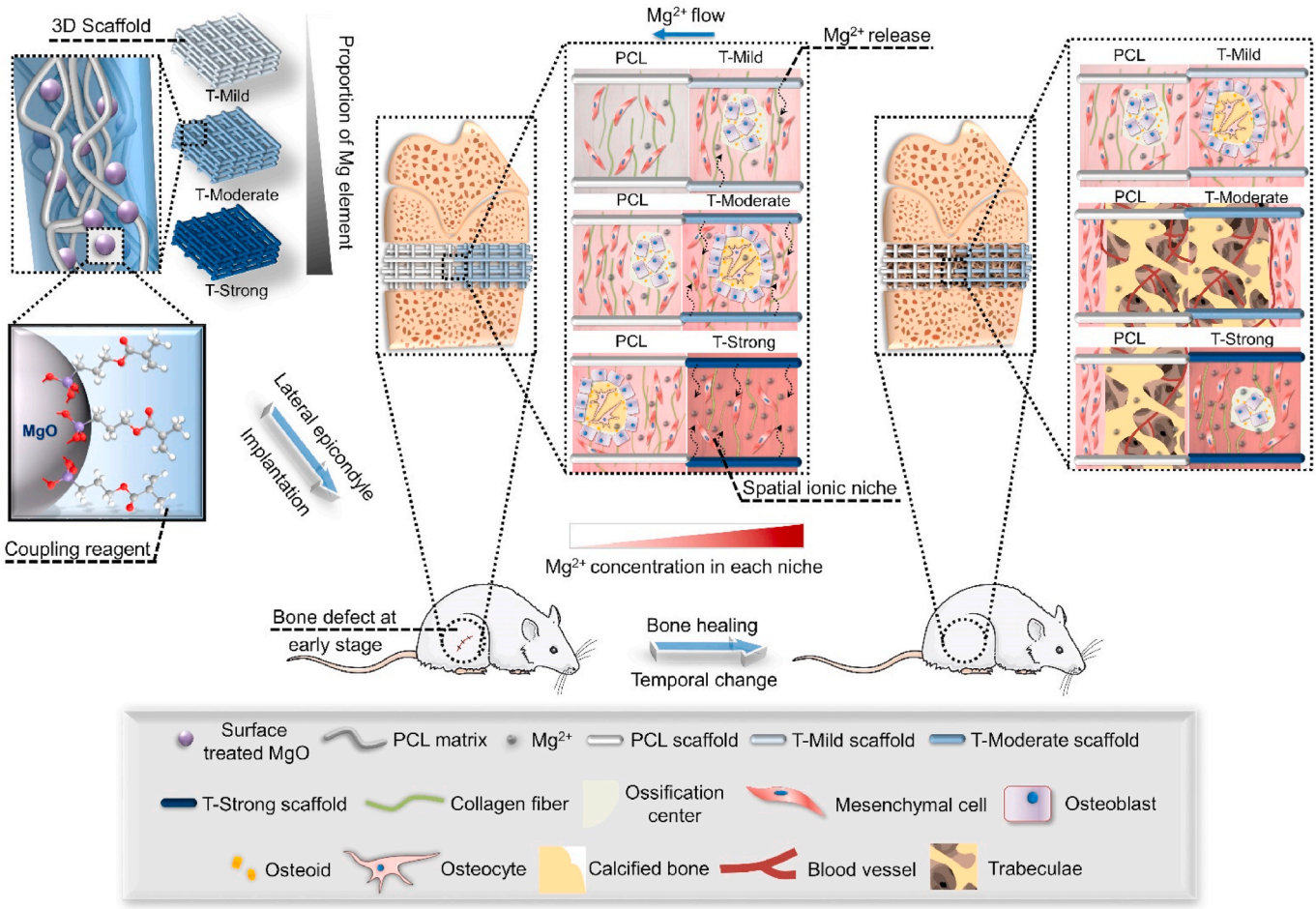

Scheme 1. Schematic diagram expounding the effect of different magnesium ionic microenvironments established by 3D scaffolds on bone tissue regeneration. A moderate Mg^{2+} niche can enhance all-stage cell performances and lead to a dramatic increase in new bone formation. Meanwhile, an Mg^{2+} deficient or excess microenvironment could be accompanied by altered cell behaviors and result in serious inhibition of the bone healing process. The scaffolds with controlled local microenvironments can significantly promote early-stage bone healing through the intramembranous ossification process when the Mg^{2+} microenvironment is properly addressed, whereas bone regeneration was rarely seen with Mg^{2+} deficiency or excess Mg^{2+}. However, when magnesium ions diffused into free Mg zone from concentrated zone with the temporal change, new bone formation on free Mg zone became significant.

regulation [71]. In combination with the data for local spatial distribution of magnesium ions (Fig. 5e), it seems clear, on the one hand, that a substrate that provides magnesium ions higher than a certain concentration could result in good cellular performance, such as superior adhesion and spreading. On the other hand, however, a magnesium ion deficient microenvironment just several micrometers away from the area with an appropriate Mg^{2+} concentration may be accompanied by altered osteoblast behavior. The reported SEM and fluoresce observations (Fig. 5c and d) of MC3T3-E1 pre-osteoblast cell morphologies presented on different co-disks were in accordance with this data. The ionic microenvironment had a very local impact such that uneven distribution of Mg^{2+} can generate a microenvironment with either a deficit or excess of magnesium ions, which lasts for a long time.

Studies of the role of Mg^{2+} in bone growth stimulation have demonstrated that the ions not only enhance bone adhesion and bone healing but also aid in the growth of bone marrow cells through the enhancement of bone morphogenetic protein (BMP)-receptor recognition, Smad signaling pathways and/or upregulation of neuronal calcitonin gene-related polypeptide-α (CGRP) [72–74]. To synthetically investigate the impact of the magnesium microenvironment on bony tissue regeneration, micro-computed tomography and histological analysis were adopted as evaluation methods for the *in vivo* study (Figs. 6–9). Typical features of intramembranous bone formation can be observed, while no intermediate cartilage was involved over the course of the bone healing; thus, the bone formation within the defect areas was confirmed to have undergone the intramembranous ossification process. Additionally, with the optimal magnesium ion release rate, T-Moderate showed the highest amount of new bone growth during the entire experimental period. It is noteworthy that the PCL scaffold from the PCL/T-Strong group also revealed a dramatic amount of new bone formation in the entire area of the defect, starting at four weeks post-operation. This may be attributed to the permeation of Mg^{2+} from the T-Strong side. Quantitative control of the microenvironments that can be obtained by designed materials that provide adhesion, growth, or migration signals are required for regeneration to succeed [75]. Although the PCL + T-Mild, PCL + T-Moderate, and PCL + T-Strong 3D-scaffolds were implanted into the same defects, scaffolds that have controlled local microenvironments can significantly promote intramembranous ossification when the Mg^{2+} concentration is properly addressed (Scheme 1).

5. Conclusion

To study the effect of magnesium ionic microenvironments on bone tissue regeneration, early-stage cellular behaviors of pre-osteoblast within mediums containing different concentrations of Mg^{2+} were first investigated. Based on the results obtained, composite materials that could provide mild, moderate or excess magnesium ions for bone

healing were then fabricated. Cellular behaviors of eGFPOB, MC3T3-E1 pre-osteoblast and human mesenchymal stem cells on different materials were studied next. Finally, an *in vivo* study was performed to synthetically investigate the impact of the magnesium microenvironment on bony tissue regeneration. The results indicated that a substrate that provides Mg^{2+} ions in concentrations higher than a certain level could result in good biological performances, such as superior cell adhesion and spreading. However, only several micrometers away from the area with an appropriate Mg^{2+} concentration, a Mg^{2+} ion-deficient or excess microenvironment could be accompanied by altered cellular behaviors. Furthermore, scaffolds with controlled local microenvironments can significantly promote early-stage bone healing through the intramembranous ossification process when the Mg^{2+} microenvironment is properly addressed, whereas bone regeneration was rarely seen with Mg^{2+} deficiency or excess Mg^{2+}. However, when magnesium ions diffused into free Mg zone from concentrated zone with the temporal change, new bone formation on free Mg zone became significant. The local tissue niche enclosed with biochemical cue, the magnesium ion, tightly orchestrates the fate of cells and subsequent tissue regeneration.

CRediT authorship contribution statement

Jie Shen: Data curation, Writing - review & editing. **Bo Chen:** Data curation, Writing - review & editing. **Kelvin W.K. Yeung:** Data curation, Writing - review & editing.

Declaration of competing interest

The authors declare that they have no known competing financial interests or personal relationships that could have appeared to influence the work reported in this paper.

Acknowledgement

Jie Shen and Bo Chen contributed equally to this work. This work was financially supported by the National key R&D Program of China (2018YFC1105100), Health and Medical Research Fund (19180712), Shenzhen Science and Technology Funds (JSGG20180507183242702), Hong Kong Innovation Technology Fund (ITS/287/17 and ITS/405/18), Hong Kong Research Grant Council General Research Fund (17214516), the Science and Technology Commission of Shanghai Municipality (18410760600), International Partnership Program of Chinese Academy of Sciences (GJHZ1850) and National Natural Science Foundation of China (81572113).

Appendix A. Supplementary data

Supplementary data to this article can be found online at https://doi.org/10.1016/j.bioactmat.2020.08.025.

References

[1] L. Dong, W.-M. Yu, H. Zheng, M.L. Loh, S.T. Bunting, M. Pauly, G. Huang, M. Zhou, H.E. Broxmeyer, D.T. Scadden, Leukaemogenic effects of Ptpn11 activating mutations in the stem cell microenvironment, Nature 539 (7628) (2016) 304.
[2] M. Levy, C.A. Thaiss, D. Zeevi, L. Dohnalova, G. Zilberman-Schapira, J.A. Mahdi, E. David, A. Savidor, T. Korem, Y. Herzig, Microbiota-modulated metabolites shape the intestinal microenvironment by regulating NLRP6 inflammasome signaling, Cell 163 (6) (2015) 1428–1443.
[3] Y. Zhou, C. Wu, J. Chang, Bioceramics to regulate stem cells and their microenvironment for tissue regeneration, Mater. Today 24 (2019) 41–56.
[4] G.F. Heidkamp, J. Sander, C.H. Lehmann, L. Heger, N. Eissing, A. Baranska, J.J. Lühr, A. Hoffmann, K.C. Reimer, A. Lux, Human lymphoid organ dendritic cell identity is predominantly dictated by ontogeny, not tissue microenvironment, Science immunology 1 (6) (2016) eaai7677.
[5] E. Jeffery, A. Wing, B. Holtrup, Z. Sebo, J.L. Kaplan, R. Saavedra-Peña, C.D. Church, L. Colman, R. Berry, M.S. Rodeheffer, The adipose tissue microenvironment regulates depot-specific adipogenesis in obesity, Cell Metabol. 24 (1) (2016) 142–150.
[6] S.F. Badylak, A scaffold immune microenvironment, Science 352 (6283) (2016) 298-298.
[7] W. Liu, X. Dan, W.W. Lu, X. Zhao, C. Ruan, T. Wang, X. Cui, X. Zhai, Y. Ma, D. Wang, W. Huang, H. Pan, Spatial distribution of biomaterial microenvironment pH and its modulatory effect on osteoclasts at the early stage of bone defect regeneration, ACS Appl. Mater. Interfaces 11 (9) (2019) 9557–9572.
[8] T. Dvir, B.P. Timko, D.S. Kohane, R. Langer, Nanotechnological strategies for engineering complex tissues, Nat. Nanotechnol. 6 (1) (2011) 13–22.
[9] K. Sadtler, K. Estrellas, B.W. Allen, M.T. Wolf, H. Fan, A.J. Tam, C.H. Patel, B.S. Luber, H. Wang, K.R. Wagner, Developing a pro-regenerative biomaterial scaffold microenvironment requires T helper 2 cells, Science 352 (6283) (2016) 366–370.
[10] S. Xiong, H. Gao, L. Qin, Y.-G. Jia, L. Ren, Engineering topography: effects on corneal cell behavior and integration into corneal tissue engineering, Bioactive materials 4 (2019) 293–302.
[11] J. Vormann, Magnesium: nutrition and metabolism, Mol. Aspect. Med. 24 (2003) 27–37.
[12] B.J.C. Luthringer, R. Willumeit-Romer, Effects of magnesium degradation products on mesenchymal stem cell fate and osteoblastogenesis, Gene 575 (1) (2016) 9–20.
[13] G. Song, Control of biodegradation of biocompatable magnesium alloys, Corrosion Sci. 49 (4) (2007) 1696–1701.
[14] W. Wang, K.W. Yeung, Bone grafts and biomaterials substitutes for bone defect repair: a review, Bioactive Materials 2 (4) (2017) 224–247.
[15] H. Zreiqat, C.R. Howlett, A. Zannettino, P. Evans, G.S. Tanzil, C. Knabe, M. Shakibaei, Mechanisms of magnesium-stimulated adhesion of osteoblastic cells to commonly used orthopaedic implants, J. Biomed. Mater. Res. 62 (2) (2002) 175–184.
[16] J.W. Park, Y.J. Kim, J.H. Jang, H. Song, Osteoblast response to magnesium ion-incorporated nanoporous titanium oxide surfaces, Clin. Oral Implants Res. 21 (11) (2010) 1278–1287.
[17] Y. Zhang, J. Xu, Y.C. Ruan, M.K. Yu, M. O'Laughlin, H. Wise, D. Chen, L. Tian, D. Shi, J. Wang, Implant-derived magnesium induces local neuronal production of CGRP to improve bone-fracture healing in rats, Nat. Med. 22 (10) (2016) 1160.
[18] L. Li, J. Gao, Y. Wang, Evaluation of cyto-toxicity and corrosion behavior of alkali-heat-treated magnesium in simulated body fluid, Surf. Coating. Technol. 185 (1) (2004) 92–98.
[19] C.M. Serre, M. Papillard, P. Chavassieux, J.C. Voegel, G. Boivin, Influence of magnesium substitution on a collagen-apatite biomaterial on the production of a calcifying matrix by human osteoblasts, J. Biomed. Mater. Res. (1998) 626–633.
[20] R.K. Rude, H.E. Gruber, H.J. Norton, L.Y. Wei, A. Frausto, J. Kilburn, Dietary magnesium reduction to 25% of nutrient requirement disrupts bone and mineral metabolism in the rat, Bone 37 (2) (2005) 211–219.
[21] Y. Toba, Y. Kajita, R. Masuyama, Y. Takada, K. Suzuki, S. Aoe, Dietary magnesium supplementation affects bone metabolism and dynamic strength of bone in ovariectomized rats, J. Nutr. 130 (2) (2000) 216–220.
[22] L. Gu, D.J. Mooney, Biomaterials and emerging anticancer therapeutics: engineering the microenvironment, Nat. Rev. Canc. 16 (1) (2016) 56.
[23] E.W. Young, D.J. Beebe, Fundamentals of microfluidic cell culture in controlled microenvironments, Chem. Soc. Rev. 39 (3) (2010) 1036–1048.
[24] A.K. Gaharwar, A. Arpanaei, T.L. Andresen, A. Dolatshahi-Pirouz, 3D biomaterial microarrays for regenerative medicine: current state-of-the-art, emerging directions and future trends, Adv. Mater. 28 (4) (2016) 771–781.
[25] D. Jhala, H. Rather, D. Kedaria, J. Shah, S. Singh, R. Vasita, Biomimetic polycaprolactone-chitosan nanofibrous substrate influenced cell cycle and ECM secretion affect cellular uptake of nanoclusters, Bioactive materials 4 (2019) 79–86.
[26] J. Shen, W. Wang, X. Zhai, B. Chen, W. Qiao, W. Li, P. Li, Y. Zhao, Y. Meng, S. Qian, X. Liu, P.K. Chu, K.W.K. Yeung, 3D-printed nanocomposite scaffolds with tunable magnesium ionic microenvironment induce in situ bone tissue regeneration, Applied Materials Today 16 (2019) 493–507.
[27] S.N. Shabala, I.A. Newman, J. Morris, Oscillations in H+ and Ca2+ ion fluxes around the elongation region of corn roots and effects of external pH, Plant Physiol. 113 (1) (1997) 111–118.
[28] O. Chaudhuri, L. Gu, D. Klumpers, M. Darnell, S.A. Bencherif, J.C. Weaver, N. Huebsch, H.-p. Lee, E. Lippens, G.N. Duda, D.J. Mooney, Hydrogels with tunable stress relaxation regulate stem cell fate and activity, Nat. Mater. 15 (3) (2016) 326–334.
[29] A.J. Keung, S. Kumar, D.V. Schaffer, Presentation counts: microenvironmental regulation of stem cells by biophysical and material cues, Annu. Rev. Cell Dev. Biol. 26 (1) (2010) 533–556.
[30] J. Rouwkema, A. Khademhosseini, Vascularization and angiogenesis in tissue engineering: beyond creating static networks, Trends Biotechnol. 34 (9) (2016) 733–745.
[31] M.M. Chelsea, L.A. Daniel, S.A. Kristi, Bio-inspired 3D microenvironments: a new dimension in tissue engineering, Biomed. Mater. 11 (2) (2016) 022001.
[32] J. Chen, X. Zou, Self-assemble peptide biomaterials and their biomedical applications, Bioactive materials 4 (2019) 120–131.
[33] H. Rubin, Central role for magnesium in coordinate control of metabolism and growth in animal cells, Proc. Natl. Acad. Sci. Unit. States Am. 72 (9) (1975) 3551–3555.
[34] A.L. Berrier, K.M. Yamada, Cell–matrix adhesion, J. Cell. Physiol. 213 (3) (2007) 565–573.
[35] B.M. Gumbiner, Cell adhesion: the molecular basis of tissue architecture and morphogenesis, Cell 84 (3) (1996) 345–357.
[36] J.-W. Park, Y.-J. Kim, J.-H. Jang, H. Song, Osteoblast response to magnesium ion-incorporated nanoporous titanium oxide surfaces, Clin. Oral Implants Res. 21 (11) (2010) 1278–1287.
[37] M.C. Siebers, P.J. ter Brugge, X.F. Walboomers, J.A. Jansen, Integrins as linker

proteins between osteoblasts and bone replacing materials, A critical review, Biomaterials 26 (2) (2005) 137–146.
[38] M. Takeichi, T.S. Okada, Roles of magnesium and calcium ions in cell-to-substrate adhesion, Exp. Cell Res. 74 (1) (1972) 51–60.
[39] J. Gailit, E. Ruoslahti, Regulation of the fibronectin receptor affinity by divalent cations, J. Biol. Chem. 263 (26) (1988) 12927–12932.
[40] L. Wu, B.J.C. Luthringer, F. Feyerabend, A.F. Schilling, R. Willumeit, Effects of extracellular magnesium on the differentiation and function of human osteoclasts, Acta Biomater. 10 (6) (2014) 2843–2854.
[41] H. Zreiqat, C.R. Howlett, A. Zannettino, P. Evans, G. Schulze-Tanzil, C. Knabe, M. Shakibaei, Mechanisms of magnesium-stimulated adhesion of osteoblastic cells to commonly used orthopaedic implants, J. Biomed. Mater. Res. 62 (2) (2002) 175–184.
[42] V.t. Boekhorst, L. Preziosi, P. Friedl, Plasticity of cell migration in vivo and in silico, Annu. Rev. Cell Dev. Biol. 32 (1) (2016) 491–526.
[43] E. Scarpa, R. Mayor, Collective cell migration in development, J. Cell Biol. 212 (2) (2016) 143–155.
[44] D.A. Lauffenburger, A.F. Horwitz, Cell migration: a physically integrated molecular process, Cell 84 (3) (1996) 359–369.
[45] E. Abed, R. Moreau, Importance of melastatin-like transient receptor potential 7 and cations (magnesium, calcium) in human osteoblast-like cell proliferation, Cell Prolif 40 (6) (2007) 849–865.
[46] J.J. Grzesiak, M.D. Pierschbacher, Shifts in the concentrations of magnesium and calcium in early porcine and rat wound fluids activate the cell migratory response, J. Clin. Invest. 95 (1) (1995) 227–233.
[47] J. Grzesiak, G. Davis, D. Kirchhofer, M. Pierschbacher, Regulation of alpha 2 beta 1-mediated fibroblast migration on type I collagen by shifts in the concentrations of extracellular Mg2+ and Ca2+, J. Cell Biol. 117 (5) (1992) 1109–1117.
[48] F. Wolf, Chemistry and biochemistry of magnesium, Mol. Aspect. Med. 24 (1) (2003) 3.
[49] S.F. Hackett, Z. Friedman, P.A. Campochiaro, Cyclic 3′,5′-adenosine monophosphate modulates vascular endothelial cell migration in vitro, Cell Biol. Int. Rep. 11 (4) (1987) 279–287.
[50] J.A.M. Maier, D. Bernardini, Y. Rayssiguier, A. Mazur, High concentrations of magnesium modulate vascular endothelial cell behaviour in vitro, Biochim. Biophys. Acta (BBA) - Mol. Basis Dis. 1689 (1) (2004) 6–12.
[51] A.H. Rubin, M. Terasaki, H. Sanui, Major intracellular cations and growth control: correspondence among magnesium content, protein synthesis, and the onset of DNA synthesis in BALB/c3T3 cells, Proc. Natl. Acad. Sci. Unit. States Am. 76 (8) (1979) 3917–3921.
[52] G.T. Rijkers, A.W. Griffioen, Changes in free cytoplasmic magnesium following activation of human lymphocytes, Biochem. J. 289 (2) (1993) 373–377.
[53] S. Ishijima, T. Sonoda, M. Tatibana, Mitogen-induced early increase in cytosolic free Mg2+ concentration in single Swiss 3T3 fibroblasts, Am. J. Physiol. Cell Physiol. 261 (6) (1991) C1074–C1080.
[54] V. Covacci, N. Bruzzese, A. Sgambato, A. Di Francesco, M.A. Russo, F.I. Wolf, A. Cittadini, Magnesium restriction induces granulocytic differentiation and expression of P27Kip1 in human leukemic HL-60 cells, J. Cell. Biochem. 70 (3) (1998) 313–322.
[55] A. Sgambato, F.I. Wolf, B. Faraglia, A. Cittadini, Magnesium depletion causes growth inhibition, reduced expression of cyclin D1, and increased expression of P27KIP1 in normal but not in transformed mammary epithelial cells, J. Cell. Physiol. 180 (2) (1999) 245–254.
[56] C.J. Sherr, Mammalian G1 cyclins, Cell 73 (6) (1993) 1059–1065.
[57] A.C. Federica I. Wolf, Magnesium in cell proliferation and differentiation, Front. Biosci. 4 (1999) d607–617.
[58] H. Rubin, The logic of the Membrane, Magnesium, Mitosis (MMM) model for the regulation of animal cell proliferation, Arch. Biochem. Biophys. 458 (1) (2007) 16–23.
[59] Y. Xie, C.A. Hill, Z. Xiao, H. Militz, C. Mai, Silane coupling agents used for natural fiber/polymer composites: a review, Compos. Appl. Sci. Manuf. 41 (7) (2010) 806–819.
[60] J.Z. Lu, Q. Wu, H.S. McNabb, Chemical coupling in wood fiber and polymer composites: a review of coupling agents and treatments, Wood Fiber Sci. 32 (1) (2007) 88–104.
[61] Y. Yuan, H. Lin, D. Yu, Y. Yin, B. Tang, E. Li, S. Zhang, Effects of perfluorooctyltriethoxysilane coupling agent on the properties of silica filled PTFE composites, J. Mater. Sci. Mater. Electron. 28 (12) (2017) 8810–8817.
[62] H.W. Nie, Y.K. Zhou, L. Yang, Y. Cao, Influence on Friction Material Performance of Nano-MMT Composites of PF by in Situ Method, Key Engineering Materials, Trans Tech Publ, 2014, pp. 8–13.
[63] A.J. Engler, S. Sen, H.L. Sweeney, D.E. Discher, Matrix elasticity directs stem cell lineage specification, Cell 126 (4) (2006) 677–689.
[64] M.P. Staiger, A.M. Pietak, J. Huadmai, G. Dias, Magnesium and its alloys as orthopedic biomaterials: a review, Biomaterials 27 (9) (2006) 1728–1734.
[65] H. Zreiqat, C. Howlett, A. Zannettino, P. Evans, G. Schulze-Tanzil, C. Knabe, M. Shakibaei, Mechanisms of magnesium-stimulated adhesion of osteoblastic cells to commonly used orthopaedic implants, J. Biomed. Mater. Res. 62 (2) (2002) 175–184.
[66] H.M. Wong, S. Wu, P.K. Chu, S.H. Cheng, K.D.K. Luk, K.M.C. Cheung, K.W.K. Yeung, Low-modulus Mg/PCL hybrid bone substitute for osteoporotic fracture fixation, Biomaterials 34 (29) (2013) 7016–7032.
[67] H.M. Wong, Y. Zhao, F.K. Leung, T. Xi, Z. Zhang, Y. Zheng, S. Wu, K.D. Luk, K. Cheung, P.K. Chu, Functionalized polymeric membrane with enhanced mechanical and biological properties to control the degradation of magnesium alloy, Advanced Healthcare Materials 6 (8) (2017).
[68] H.M. Wong, Y. Zhao, V. Tam, S. Wu, P.K. Chu, Y. Zheng, M.K.T. To, F.K. Leung, K.D. Luk, K.M. Cheung, In vivo stimulation of bone formation by aluminum and oxygen plasma surface-modified magnesium implants, Biomaterials 34 (38) (2013) 9863–9876.
[69] F.D. Marzia Leidi, Massimo Mariotti, Jeanette A.M. Maier, High magnesium inhibits human osteoblast differentiation in vitro, Magnes. Res. 24 (1) (2011) 1–6.
[70] K. Yusa, O. Yamamoto, H. Takano, M. Fukuda, M. Iino, Zinc-modified titanium surface enhances osteoblast differentiation of dental pulp stem cells in vitro, Sci. Rep. 6 (2016).
[71] C.A. DeForest, B.D. Polizzotti, K.S. Anseth, Sequential click reactions for synthesizing and patterning 3D cell microenvironments, Nat. Mater. 8 (8) (2009) 659–664.
[72] Y. Zhang, J. Xu, Y.C. Ruan, M.K. Yu, M. O'Laughlin, H. Wise, D. Chen, L. Tian, D. Shi, J. Wang, S. Chen, J.Q. Feng, D.H.K. Chow, X. Xie, L. Zheng, L. Huang, S. Huang, K. Leung, N. Lu, L. Zhao, H. Li, D. Zhao, X. Guo, K. Chan, F. Witte, H.C. Chan, Y. Zheng, L. Qin, Implant-derived magnesium induces local neuronal production of CGRP to improve bone-fracture healing in rats, Nat. Med. 22 (10) (2016) 1160–1169.
[73] S. Ding, J. Zhang, Y. Tian, B. Huang, Y. Yuan, C. Liu, Magnesium modification upregulates the bioactivity of bone morphogenetic protein-2 upon calcium phosphate cement via enhanced BMP receptor recognition and Smad signaling pathway, Colloids Surf. B Biointerfaces 145 (2016) 140–151.
[74] S. Yoshizawa, A. Brown, A. Barchowsky, C. Sfeir, Magnesium ion stimulation of bone marrow stromal cells enhances osteogenic activity, simulating the effect of magnesium alloy degradation, Acta Biomater. 10 (6) (2014) 2834–2842.
[75] M.E. Davis, P.C.H. Hsieh, A.J. Grodzinsky, R.T. Lee, Custom design of the cardiac microenvironment with biomaterials, Circ. Res. 97 (1) (2005) 8–15.